Determining the spectroscopic quadrupole moment of the first 2^+ state in ^{36}Ar

Elias Jose Martin Montes

UNIVERSITY *of the*
WESTERN CAPE

A thesis is submitted in fulfilment of the requirements
of the Masters in Science degree
in the Department of Physics and Astronomy,
University of the Western Cape.

Supervised by:
Prof. J.N. Orce, University of the Western Cape.
March 12, 2019

Declaration

I declare that *Determining the spectroscopic quadrupole moment of the first 2+ state in 36Ar* is my own work, that it has not been submitted for any degree or examination in any other university, and that all the sources I have used or quoted have been indicated and acknowledged by complete references.

Full name: ELIAS JOSE MARTIN MONTES

Signed: Date: 12/03/2019

Abstract

A series of reorientation-effect Coulomb-excitation experiments were carried out at iThemba LABS from April to May 2016. Enriched ion beams of ^{40}Ar, ^{36}Ar and ^{32}S were bombarded at safe energies, well below the Coulomb barrier, onto a heavy^{194}Pt target with thickness 1mg/cm^2. The three experiments were performed to determine the spectroscopic or static quadrupole moment Q_s, of the first excitation 2_1^+ in these nuclei in order to shed light on the zip-zap of nuclear shapes found at the end of the *sd* shell. This thesis will be dealing with the particular case of ^{36}Ar, accelerated at a safe bombarding energy of 134.2 MeV. For this purpose, a particle-gamma coincidence experiment has been carried out using the AFRODITE array – composed of 8 high-purity germanium clover detectors – to detect the de-exciting gamma energies, coupled to a double-sided CD-type S3 silicon detector at backward angles – composed of 32 sectors and 24 rings – to detect the scattering particles. A new optimised sorting code has been developed which included fast computing processing, non-Doppler (^{194}Pt) and Doppler correction (^{36}Ar), add-back, and energy-sharing, particle and time tagging conditions. The peaks of interests in the spectra were analysed using the Coulomb-excitation code GOSIA. Using the normalization method, a more precise determination of $Q_s(2_1^+) = +0.09(3)$ eb has been accomplished.

Acknowledgements

I would like to thank my good friend and supervisor, Prof Nico Orce, as well as the University of the Western Cape (Prof Lorna Holtman in particular), University of Toulouse III and iThemba LABS for the opportunity they have given me to carry out this MSc in Nuclear Physics and because without their great support I would not have never achieved to carry out this thesis and be trained in this exciting field.

I do not want to forget to mention the gratitude too to the UWC COULEX group and my family for putting up with me for the whole period. It is always good to remember the Sharambulleiros ethos: "Ser el mejor no lo es todo, pero alguien tiene que serlo".
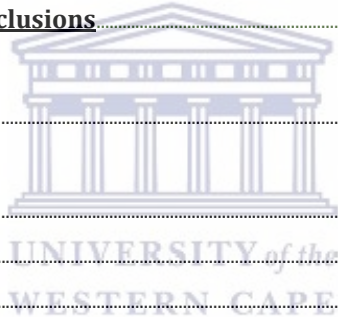
Table of Contents

Contents

List of Figures

List of Tables

UNIVERSITY *of the*
WESTERN CAPE

1 Introduction

One of the central goals of nuclear-structure physics is to infer a basic understanding of the structure and dynamics of nuclei. Besides, how the strong force binds these nucleons together in nuclei is fundamental to the very existence of the universe. In the same way that electron beams were used to determine the atomic structure, nowadays one of the best ways to determining and understanding the nucleus is by using stable and radioactive ion beams for the excitation of the nucleus. One of these methods is the Coulomb excitation.

Around the world various research groups are working actively on Coulomb-excitation experiments in order to understand the collective behaviour of the nucleus and the interaction between the proton and nuetrons. With the advancement of accelerator technologies, it is possible to find facilities for these kinds of experiments. iThemba LABS in South Africa, is one of these state-of-the-art facilities where it is possible to perform Coulomb-excitation experiments with a stable beam impinging onto a stationary target.

For the measurements presented here, the de-exciting γ rays were collected using 8 clover detectors, five at 90º and three at 135º, in the AFRODITE array. Information from the scattered particles was extracted using a double-sided S3 CD-type silicon detector from Micron Semiconductors and placed at backward angles, covering a scattering angular range between 131.3^o and 157.6^o.

The detailed experimental procedure for the current work is discussed in chapter 3, followed by data analysis in chapter 4 and discussion of the results in chapter 5. In this and in the next chapters, the scientific motivation of the experiment, the theoretical aspect of Coulomb-excitation perturbation theory and the reorientation-effect in Coulomb-excitation (RECE) procedure, to determine spectroscopic quadrupole moments, are discussed.

3

1.1 Scientific motivation

The spectroscopic quadrupole moment of the 2_1^+ state, $Q_s(2_1^+)$, in $^{36}_{18}$Ar has been determined using the reorientation effect in Coulomb-excitation (RECE). The experiment was performed at safe energies, i.e. at bombarding energies well below the Coulomb barrier, where nuclear interactions are assumed to be negligible. Nakai *et al*. had previously reported $Q_s(2_1^+) = +0.11 \pm 0.6$ eb for ^{36}Ar **[1]**. This remains the only RECE measurement of $Q_s(2_1^+)$ in ^{36}Ar and the accepted value in the NNDC (National Nuclear Data Center) **[2].** This value may be questionable as the measurement was done at clearly unsafe energies, with a minimum separation between nuclear surfaces of $S(\theta)_{c.m.}$min = 4.3. In addition, $Q_s(2_1^+)(^{206}_{82}Pb) = (0.0 \pm 0.5)|Q^{rot}|$ was assumed for the normalization of the data. This presents a big discrepancy with the value reported by Spear, where $Q_s(2_1^+)(^{206}_{82}Pb) = (0.17 \pm 0.31)|Q^{rot}|$ was determined **[3].**

Only experimental determination of $Q_s(2_1^+)$ for $^{36}_{18}Ar(E_x = 1.970 MeV)$ using RECE and $^{36}_{18}Ar$ projectiles

Nucleus	Authors	Year	$Q_{2^+}(e\,fm^2)$	Target	Details	$S_{min}\,(fm)$
$^{36}_{18}$Ar	Nakai et al.	1971	$+11 \pm 6$	$^{206}_{82}Pb$	$P_\gamma C;\ \theta = 90^o, 160^o;\ assumes$	4.6
					$Q_{2^+}(^{206}_{82}Pb) = (0.0 \pm 0.5)|Q_2^{rot}|$	

Table 1: The $Q_s(2_1^+)$ value of $^{36}_{18}Ar$ obtained by Nakai and collaborators **[1].**

In the early implementation of the RECE **[4]**, the de-excited γ rays were detected using NaI(Tl) detectors. Current advances in detector technology offer high-resolution detector systems such as high-purity germanium (HPGe). These detectors offer a much better resolution, and if segmented, a more enhanced Doppler-effect capability correction compared to NaI(Tl) detectors.

Using the AFRODITE array available at iThemba LABS with a safe energy beam of $E_{lab} = 134.2(5)$ MeV at $S(\theta)_{c.m.}$min = 6.5 fm, an improved measurement of the $Q_s(2_1^+)$ value was performed. Furthermore, the use of a heavy target as $^{194}_{78}$Pt enhances the sensitivity of the RECE because of its proportional dependence with the proton number of the target.

4

Once an improved $Q_s(2_1^+)$ value had been obtained it would possibly shed light onto the zig-zag pattern between oblate and prolate shapes at the upper part of the sd shell before a small $Q_s(2_1^+)$ value is observed near the end of the shell ($_{18}^{40}Ar$), as shown in Figure 1. This tendency pattern of measured $Q_s(2_1^+)$ values in the sd shell begins with a nearly-spherical shape in $_8^{18}O$, rapidly changing to large prolate deformations($Q_s(2_1^+) < 0$) before drastically flipping to a large oblate ($Q_s(2_1^+) > 0$) deformation in $_{14}^{28}Si$. From this point onwards, the quadrupole shapes oscillate in a zig-zag pattern. The reason to use backward angles in this experiment is because the sensitivity between different Q_s values is largest **[5]**.
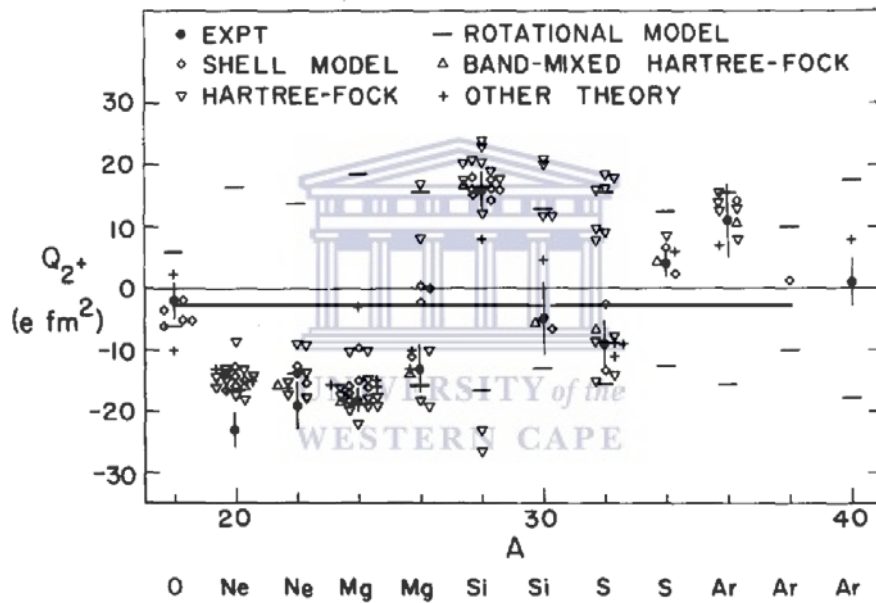
Figure 1: Experimental (RECE) and theoretical $Q_s(2_1^+)$ values in the *sd* shell **[3].**

Although for technical reasons some parameters of this experiment were changed when it was carried out, the preliminary research proposal of this experiment can be found in Appendix C. The small changes of some parameters account for different heavy target and the beam energy. The scientific motivation has not changed at all.

2 Coulomb Excitation

Nuclear excitation caused solely by the electromagnetic field acting between the colliding atomic nuclei following Rutherford scattering is called Coulomb excitation (or Coulex). That is the electro-magnetic excitation process occurring when a nucleus is passing at close distance by another nucleus and thus experiencing a time-dependent electromagnetic field.

When the excitation of nuclei is induced by the bombarding projectile at beam energies well below the Coulomb barrier and the separation between nuclear surfaces is large enough (6.5 fm for light nuclei and 5 fm for heavy ions), nuclear interference can be considered negligible. It can then be said that the Coulomb excitation occurs at a safe energy, so called `safe Coulex'. In this case, the projectile and target nuclei interact solely through the electromagnetic interaction **[6]**. Coulomb excitation at safe energies is a very powerful probe to excite the collective degrees of freedom of the nucleus. Besides, in the case of pure Coulomb excitation, the excitation probability can be exactly calculated using a semi-classical approximation, which allows the extraction of electro-magnetic transition probabilities between different states and their static moments.

One of the most important aspects of Coulomb excitation at safe energies is the different population of magnetic substates depending on the spectroscopic quadrupole moment of the state. This is referred as the "reorientation effect". Such a difference in the population of magnetic substates **[5],** depending on whether the state is oblate, prolate or spherical, provides a means to determine Q_s values of states with $J \neq 0, 1/2$ by measuring the cross section or integrated γ-ray yields as a function of scattering angle **[6]**, **[7]**. That is, by measuring these multipole moments, the quadrupole shape of the charge distribution in the laboratory frame can be defined as the deviation from a spherical charge distribution.

The intrinsic quadrupole moment Q_0 in the body-fixed frame is defined as,

$$Q_0 = \int \rho(3z^2 - r^2)\, dV \,, \qquad\qquad (2.1)$$

where ρ is the charge density of the infinitesimal volume dV, r is the distance from the origin to dV, and z is the projection of r onto the 3-axis. Q_0 values are one of the most relevant properties of nuclei, it gives information on the charge distribution in the intrinsic frame of the nucleus. If $Q_0 = 0$, the nucleus is spherical, it has a prolate shape if $Q_0 > 0$, or an oblate form if $Q_0 < 0$. The model-independent way to determine Q_0 requires the use of rotational invariants and an abundant set of matrix elements [7, 8]. Electric quadrupole moments are usually expressed in units of efm^2 or eb, where $b = 10^{-28}\ m^2$, which generally have a magnitude between 0 and 0.5 eb.

Figure 2: Prolate (left), spherical (middle) and oblate (right) nuclear shapes according to their intrinsic quadrupole moment, Q_0.

The reorientation-effect (RE) [10] is a model-independent way to determine the nuclear charge distribution in the laboratory frame, i.e., the spectroscopic or static quadrupole moments, Q_s. The RE generates a time-dependent hyperfine splitting of the nuclear levels, which depends on the shape of the nuclear state.

The angular distribution of the de-excited γ-rays as a function of scattering angle may be enhanced $(Q_s(2_1^+) > 0)$ or inhibited $(Q_s(2_1^+) < 0)$, hence providing a spectroscopic probe for the measurement of Q_s. From Q_s, the extraction of the charge distribution, or the intrinsic quadrupole moment Q_0 in the body-fixed

frame, is model-dependent and assumes a particular K quantum number. Most experimental methods measure the value of Q_s. Assuming an ideal axially-symmetric rotor, the relationship between thequadrupole moments is,

$$Q_s = \frac{3K^2 - I(I+1)}{(I+1)(2I+3)} Q_0 \,,$$ (2.2)

where the K quantum number is the projection of the total angular momentum I onto the symmetry axis 3 in the intrinsic coordinate system, as shown in Fig. 3.
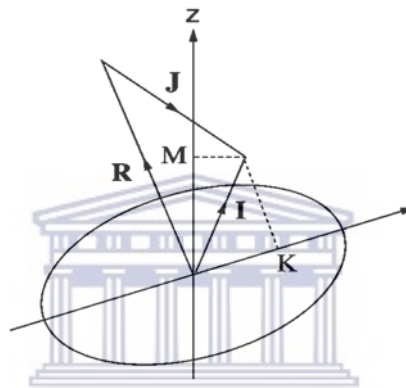
Figure 3: The K quantum number in an axially-deformed nucleus.

Finally, $Q_s(2_1^+)$ and the diagonal matrix element $\langle 2_1^+ ||E2||2_1^+ \rangle$ are related by,

$$Q_s(2_1^+) = 0.75793 \, \langle 2_1^+ ||E2||2_1^+ \rangle \,.$$ (2.3)

This chapter will describe briefly the main features of the coulomb excitation theory.

2.1 Rutherford Scattering

Ernst Rutherford in 1911 discovered the atomic nucleus **[11]** by analysing the scattering of α particles by gold nuclei. The experiment was carried out by his students, Geiger and Marsden, under his supervision. The results of this experiment replaced the previous theory of the atom by Thomson called the

"plum pudding model". The elastic Coulomb scattering of charged particles by the atomic nucleus is known as Rutherford scattering.
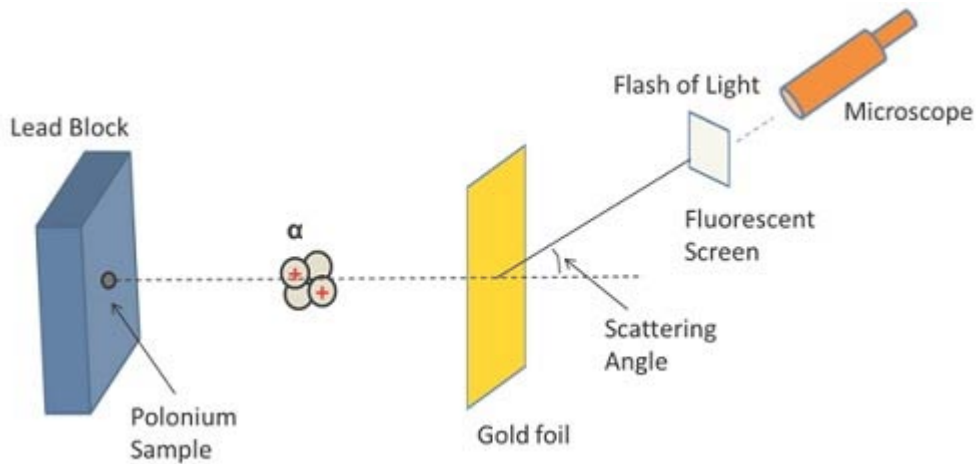
Figure 4: Rutherford's alpha scattering experiment that supported the modern image of the atomic nucleus.

In the Rutherford experiment, the α particles were emitted by a radioactive sample and collimated using a lead block, the focused beams of radiated α particles were made to impinge upon a very thin gold foil. A fluorescent screen and microscope were then used to count the number of scattered particles at different angles. The α particles were also detected at angles that were too large to be explained by the prevailing model of Thomson. Based on these surprising results, Rutherford postulated the atomic nucleus.

According to Rutherford, the atom would contain a nucleus of charge Ze, where Z is the atomic number of the atom and e the magnitude of the electric charge of an electron, and the nucleus could be treated as a point particle compared with the whole atom. The mass of the nucleus compared to the incident particle is large enough such that the nuclear recoil can be ignored. Moreover, considering the collision to be elastic, only laws of classical mechanics and electromagnetism are applicable to this phenomenon.

Consider the situation in which the incident particle hits the nucleus head-on. Let E_{cm} be the kinetic energy of the projectile in the center of mass frame and Ze its electric charge. The distance of closest approach D is then obtained by equating the initial kinetic energy T to the Coulomb potential energy at distance D,

$$D = \frac{Z_1 Z_2 e^2}{4\pi\epsilon_0 T} \ , \tag{2.4}$$

where Z_1 and Z_2 are the number of protons in the projectile and the target nuclei, respectively.

Such a collision would result in α particles reversing direction, i.e. the scattering angle ϑ in the center of mass frame would be equal to π. This case of head-on collision is a special one and the simplest case of collision between two particles.

For handling complicated cases of different scattering angles this is very useful because the analysis of the system is greatly simplified when the coordinate system is chosen to be at rest with respect to the center of mass.

By using the precedent simplification of the system of collision particles, it may be said that: when a projectile of mass M_1, charge $+Z_1 e$ and velocity υ interacts with a stationary target nucleus of mass M_2 and charge $+Z_2 e$, they both experience a long-range charge-dependent repulsive Coulomb force given by,

$$\vec{F} = \frac{1}{4\pi\epsilon_0} \frac{Z_1 Z_2 e^2}{r^2} \frac{\vec{r}}{r} \ , \tag{2.5}$$

and the potential energy associated with the force is given by,

$$V = \frac{1}{4\pi\epsilon_0} \frac{Z_1 Z_2 e^2}{r} \ , \tag{2.6}$$

where r is the radial distance separating the two nuclei. If the reaction potential in equation (2.6) is smaller than the potential barrier, the interaction results in either elastic (Rutherford) or inelastic (Coulomb-excitation) scattering.

In the case of Rutherford scattering, both the target and the projectile remain in their ground state without γ-ray emission, with the large elastic peak typically

shown in particle spectra. In Coulomb excitation, the collision could result in the excitation of both the target and projectile exciting nuclear states and leading to γ-ray emission; hence, inelastic peaks would come out in both the particle and gamma-ray spectra.
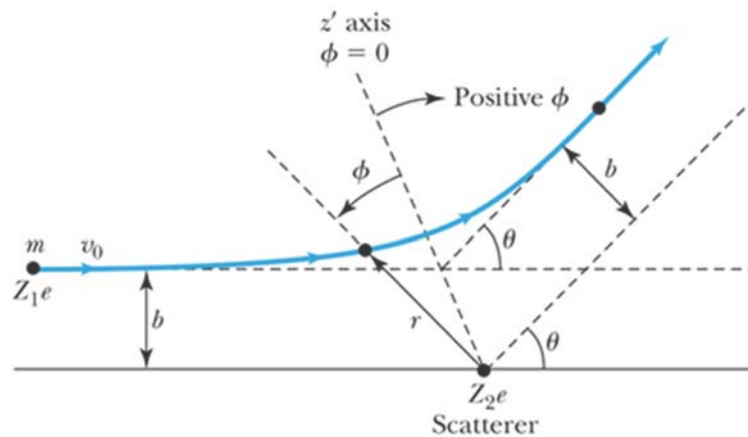
Figure 5: Schematic of the projectile motion along the Coulomb field of the target.

Figure 5 represents two important parameters of scattering, the impact parameter b and the scattering angle ϑ in the laboratory frame. The impact parameter b is the distance between nuclear centers of masses of a pair of colliding nuclei. The scattering angle is the angle through which a scattered particle or beam is deflected with respect to the center of mass. In addition, it is possible to see that because of the repulsive Coulomb forces, the scattered projectile follows a hyperbolic trajectory in concordance with the inverse square law, $1/r^2$ embodied in equation (2.5).

In an elastic collision, the linear momentum associated changes only in direction and not in magnitude. If the mass of the target M_2 is much greater than the mass of the projectile M_1, the magnitude of both the initial and final momentum of the projectile far from the target are equal, Mv, and the target nucleus is assumed to remain stationary after the collision. The change in momentum during collision can be represented as,

$$\Delta p = 2Mv sin\frac{\vartheta}{2} \ ,$$
(2.7)

11

which is considered to be equal to the net impulse due to the component of $\vec{F}$ in the same direction and can be deduced as,

$$\Delta p = \int dp = \int \vec{F} dt = \frac{Z_1 Z_2 e^2}{4\pi\epsilon} \int \frac{cos\phi}{r^2} dt, \tag{2.8}$$

where $t \in (0,\infty)$ and $\phi \in \left(-\frac{1}{2}(\pi - \vartheta), \frac{1}{2}(\pi - \vartheta)\right)$ and υ is the initial velocity of the projectile in the laboratory frame. If the solution to equation (2.8) is introduced into equation (2.7), the following relation between the parameters b and ϑ can be obtained.

$$b = \frac{a}{2} cot\frac{\vartheta}{2} . \tag{2.9}$$

The relationship between the impact parameter, scattering angle and the Rutherford cross-section $\frac{d\sigma_R}{d\Omega}$ (see section 2.2), is importance because it can be varied to establish a hyperbolic trajectory of the projectile motion. The parameter a, is defined as the half-distance of closest approach in a head-on collision (see figure 4). It can be determined by equating the kinetic and potential energies in the center of mass frame:

$$\left.\begin{aligned} E_{cm} = V_{cm} = \frac{1}{2}\mu\upsilon^2 = \frac{Z_1 Z_2 e^2}{b} \\ a = \frac{b}{2} \end{aligned}\right\} \qquad a = \frac{Z_1 Z_2 e^2}{\mu\upsilon^2} , \tag{2.10}$$

where e^2 = 1.44 MeV·fm and μ is the reduced mass,

$$\mu = \frac{M_1 M_2}{M_1 + M_2}. \tag{2.11}$$

2.2 Rutherford scattering cross-section

The expression for $b(\vartheta)$ given in equation (2.7) represents that the Rutherford differential cross-section can be deduced by considering the probability of scattering between ϑ and $\vartheta + d\vartheta$. This probability will be proportional to the area of a ring of radius b, and thickness, db, in which case $d\sigma_R/d\Omega$ in the center of mass frame is given by [6]:

$$\frac{d\sigma_R}{d\Omega} = \left(\frac{a}{2}\right)^2 \frac{1}{\sin^4\frac{\vartheta}{2}}. \qquad (2.12)$$

2.3 Collision Parameters

Apart from the scattering angle and the impact parameter, there are another three important collision parameters, depending on the reaction species and energy conditions. These are used to quantify the Coulomb-excitation process. These three collision parameters are: The Sommerfeld parameter η, the adiabaticity parameter ξ and the excitation strength parameter χ. These three parameters will be discussed in this section. The magnitudes of these parameters justify the semi-classical approximation which has been used in the analysis for the Coulomb-excitation data. In this approach, the relative motion of the colliding nuclei is considered to follow classical hyperbolic orbits, whilst the excitation progress itself is treated with quantum mechanical considerations.

2.3.1 The Sommerfeld parameter

If the semi-classical approximation is to be rendered valid, the Coulomb field between the colliding nuclei must ensure that the projectile nucleus does not penetrate the target nucleus. In order to meet this requirement, the de Broglie wavelength ($\lambda = \frac{\lambda}{2\pi}$) must be smaller than the distance of closest approach in a head-on collision, b, between the nuclei. This principal requirement is embodied in the definition of the Sommerfeld parameter:

13

$$\eta = \frac{b}{2\lambda} = \frac{Z_1 Z_2}{\hbar v} \cdot \frac{e^2}{4\pi\epsilon_0}. \tag{2.13}$$

Above, in the definition of Sommerfeld parameter, Z_1 and Z_2 denote the atomic numbers of the projectile and the target nucleus, respectively, v is the initial velocity of the projectile in the laboratory frame, $\hbar = \frac{h}{2\pi}$ and $\frac{e^2}{4\pi\epsilon_0} = 1.44$ MeV $\cdot$ fm.

Provided that η is very large compared to unity (η>>1), the scattering progress may be described in terms of quantum mechanical wavepackets with dimensions that are small in comparison to the dimensions of the classical hyperbolic orbit and thus the wavepacket can be expected to follow a classical trajectory quite accurately, and the semi-classical approximation is thus a valid treatment of the excitation mechanism.

2.3.2   The adiabaticity parameter

A further requirement of the semi-classical approximation is that the energy loss experienced by the projectile (ΔE_{if}) during collision with the target is small compared to the center-of-mass bombarding energy, (E_{cm}) of the projectile. That is, if the $\frac{\Delta E_{if}}{E_{cm}} \ll 1$ condition is met, then it can be assumed that the energy transfer during the collision does not modify the classical trajectory significantly, and the energy loss during excitation may be neglected [12, 4].

$$\Delta E_{if} = E_i - E_f, \tag{2.14}$$
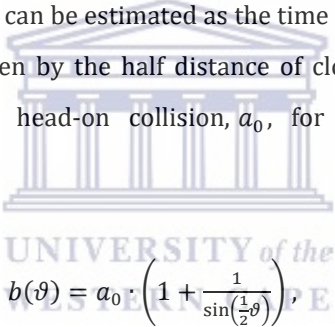
$$E_{cm} = \frac{1}{2}mv^2. \tag{2.15}$$

Under the influence of the time-dependent electromagnetic potential $V(\vec{r}\,(t))$, it is then possible to excite a nucleus from an initial state $|i\rangle$, provided that the collision time t is shorter (or of the same order) than the lifetime of the level τ, $i.e.$ $t \lesssim \tau$, where $\tau = \hbar / \Delta E_{if}$. The adiabaticity parameter ξ can be then defined as,

$$\xi = \frac{\tau}{\Delta t} = \tau \cdot \frac{\Delta E_{if}}{\hbar} \ . \tag{2.16}$$

This adiabaticity parameter ξ measures the extent to which the collision process is of ``sudden impact''. In order to meet the requirements for the semi-classical approximation, the condition $\xi \lesssim 1$ needs to be fulfilled.

The nuclear collision time can be estimated as the time taken for the projectile to travel a distance (ϑ), given by the half distance of closest approach (between nuclear centroids) in a head-on collision, a_0, for a given center-of-mass scattering angle ϑ,

$$b(\vartheta) = a_0 \cdot \left(1 + \frac{1}{\sin\left(\frac{1}{2}\vartheta\right)} \right), \tag{2.17}$$

$$a_0 = \frac{1}{2} \cdot \frac{Z_1 Z_2}{E_{cm}} \cdot \frac{e^2}{4\pi\epsilon_0} \ . \tag{2.18}$$

The collision time can then be defined as a function of scattering angle:

$$\tau(\vartheta) = \frac{d(\vartheta)}{2v} = \frac{a_0}{2v} \cdot \left(1 + \frac{1}{\sin\left(\frac{1}{2}\vartheta\right)} \right). \tag{2.19}$$

By combining equations (2.14) and (2.17) above, the adiabaticity parameter ξ can be given as function of ϑ and ξ_0, being $\xi_0 = \xi(\vartheta = \pi) = \frac{a_0 \Delta E_{if}}{v\hbar}$:

15

$$\xi = \frac{a_0 \Delta E_{if}}{2v\hbar} \cdot \left(1 + \frac{1}{\sin\left(\frac{1}{2}\vartheta\right)}\right) = \xi_0 \frac{1}{2} \cdot \left(1 + \frac{1}{\sin\left(\frac{1}{2}\vartheta\right)}\right). \qquad (2.20)$$

By substituting the equation (2.18) for a_0 above and combining with equation (2.14) one obtains the following ratio in terms of ξ and η :

$$\frac{\Delta E_{if}}{E_{cm}} = \frac{2\xi_0}{\eta}. \qquad (2.21)$$

For the most of the heavy-ion collisions cases at low-energy Coulomb excitation, the conditions $\eta \gg 1$ and $\xi \lesssim 1$ are usually satisfied, and according to equation (2.21), this implies that the requirement $\frac{\Delta E_{if}}{E_{cm}} \ll 1$ for a semi-classical description is usually fulfilled.

2.3.3 The excitation strength parameter

Along with the degree of adiabaticity, the magnitude of the excitation is also dependent upon the strength of the interaction. A dimensionless quantity, the excitation strength parameter $\chi^{(\lambda)}$, represents a measure of the strength of the multipole interaction of order λ. An explicit definition of this parameter is given in [4], which for electric transitions may be represented as:

$$\chi^{(\lambda)} = \frac{\sqrt{16\pi}(\lambda-1)!}{(2\lambda+1)!!} \cdot \frac{Z_1 e}{a_0^\lambda \hbar v} \cdot \frac{\langle I_f || M(E2) || I_i \rangle}{\sqrt{2I_i+1}}, \qquad (2.22)$$

where for electric transitions the term $\langle I_f || M(E2) || I_i \rangle$ is the reduced matrix element coupling the nuclear states $|i\rangle$ and $|f\rangle$. The strength of the interaction can be estimated by the value of the time-dependent potencial acting at the point of closest approach in a head-on collision with $\vartheta = \pi$, i.e. $(r(t)) = V(d(\pi; t))$, according to $\chi^{(\lambda)} \approx \frac{V(d(\pi))t}{2\hbar}$, with t being the collision time. The strength parameter $\chi^{(\lambda)}$ is an estimate of number of quanta of angular momentum $\lambda\hbar$ exchanged during the collision.

16

For beam energies below the Coulomb barrier, an upper limit on the value of $\chi^{(2)} \lesssim 10$ is found for electric quadrupole transitions **[12]**. The excitation strength parameter becomes around two orders of magnitude smaller for the higher $\lambda > 2$ multipolarities. Large χ and small ξ result in the state of interest being strongly exited. Hence, higher-order multipoles yield much smaller χ values, and result in very little excitation of the final state. To a very good approximation, the influence of higher-order multipoles can thus be neglected in the Coulomb-excitation calculations for the systems considered in this thesis. For $\vartheta = \pi$ and $\xi = 0$, the excitation probability is given by $|\chi|^2$. The strength parameter $\chi^{(\lambda)}$ imposes the following additional condition regarding the applicability of the semi-classical approach:

$$\frac{\chi^{(\lambda)} \lambda}{\eta} \ll 1 . \qquad (2.23)$$

This condition is usually satisfied in most heavy-ion collisions because $\eta \gg 1$. Besides, if this condition is not fulfilled, then the angular momentum transfer in the collision will have a bearing on the kinematics of the hyperbolic orbit.

2.4   Safe Coulomb-excitation requirement

As discussed in the introduction of this chapter, it is important that the excitation mechanism is purely electromagnetic in order to avoid the elusive nuclear interaction. As the Coulomb-excitation probability rapidly increases with increasing projectile energy, it is therefore desirable to utilise the highest possible bombarding beam energy, but always taking into account the previous requirement that the excitation progress must remain purely electromagnetic. Since the nuclear interaction has a very short range, only a few fm, while the Coulomb interaction is long ranged, this requirement is satisfied by ensuring that the two colliding nuclei remain outside the range of the nuclear force for every scattering angle subsequent to the collision.

For this previous condition of "safe" projectile energy to be realised, the maximum "safe" bombarding energy of the projectile has to be well below the maximum height of the Coulomb barrier [3, 5]. Systematic studies of Coulomb-nuclear interference effects have been carried out to estimate the maximum "safe" bombarding energy, E$_{max}$, involving the masses and charges of the interacting nuclei [5]. The safe bombarding energies for any projectile and target combination can be calculated using the classical expression of the minimum distance separating the nuclear surfaces $S(\vartheta)_{min}$ in equation

$$D = \frac{Z_1 Z_2 e^2}{4\,\pi\epsilon_0 T}\ . \tag{2.4}$$

Earlier, Schwalm *et al.*, [13] and Alder *et al* [6] described 3 fm and 2.88 fm respectively for this safety distance between nuclei. Experimentally, Cline *et al.* [9] estimated a $S(\vartheta)_{min} > 5.1\,fm$ for "safe" heavy-ion Coulomb excitation. Kean [7] and Spear [3] were more conservative giving $S(\vartheta)_{min} \gtrsim 6.5\,fm$ for Coulomb-excitation measurements involving light nuclei.

$$S(\vartheta)_{min} = \frac{0.72 \cdot Z_1 Z_2}{E_{max}} \left(1 + \frac{A_1}{A_2}\right)\left[1 + \csc\left(\frac{1}{2}\vartheta\right)\right] - 1.25\left(A_1^{\frac{1}{3}} + A_2^{\frac{1}{3}}\right) fm\,. \tag{2.24}$$

The previously equation (2.24) assumes a nuclear radius given by $R_{i=1,2} = r_0 A_i^{\frac{1}{3}}$, being $r_0 = 1.25$ fm and it represents the equilibrium separation of the nucleus. Thus, a measure of the minimum distance d_{min}, for which the excitation is purely electromagnetic can be calculated from $S(\vartheta)_{min}$.

$$d_{min} \geq 1.25\left(A_1^{\frac{1}{3}} + A_2^{\frac{1}{3}}\right) + S(\vartheta)_{min}. \tag{2.25}$$

As a summary and based on previous considerations, the excitation process can be obtained through the semi-classical approximation assuming that the projectile follows the classical hyperbolic trajectory and using a quantum-mechanical treatment for the nuclear excitation.

2.5   Time-dependent perturbation theory

In section 2.2, the Rutherford differential cross-section associated with the projectile motion could be described by:

$$\frac{d\sigma_R}{d\Omega} = \left(\frac{a}{2}\right)^2 \frac{1}{sin^4\frac{\vartheta}{2}} \; . \tag{2.26}$$

If during the collision, the nucleus undergoes a transition from the ground state |i⟩ to a final state |f⟩, the Coulomb-excitation cross-section may be related to the Rutherford cross section by $d\sigma_f = P_{if}d\sigma_R$, where P_{if} is the probability that a nucleus is excited in a collision in which the particle is scattered into the solid angle $d\Omega$.

The probability P_{if} for excitation of a nucleus from the ground state with spin I_i to the final state I_f can be expressed as:

$$P_{if} = \frac{1}{2I_i+1}\sum\nolimits_{M_iM_f} |b_{if}|^2 \; , \tag{2.27}$$

where b_{if} are the transition amplitudes, M_i and M_f the magnetic substates quantum numbers of the initial and final states, respectively. The perturbation treatment of the semi-classical approximation provides an understanding of the excitation process. The probability P_{if} that one nucleus is exited in a collision using Coulomb excitation of light ions is less than unity, therefore a first-order perturbation treatment of the excitation process may be adequate. In the case of using heavy target, second or higher order terms enhances the perturbation expansion of the Coulomb-excitation cross section.

It is also well known that the symmetrized parameters - assuming initial and final values before and after collision, i.e. v_i and v_f as the initial and final velocity of the projectile, respectively - for the half distance of closest in a head-

19

on collision, a_{if}, and the adiabaticiy parameter, ξ_{if} , provide a better description of the Coulomb interaction:

$$a_{if} = \frac{Z_1 Z_2 e^2}{\mu v_i v_f},$$
(2.28)

$$\xi_{if} = \frac{a_{if} \Delta E_{if}}{\hbar} \left(\frac{1}{v_f} - \frac{1}{v_i} \right).$$
(2.29)

2.5.1 First-Order Perturbation Treatment

The excitation amplitudes of Coulomb-excited states can be evaluated using first-order perturbation theory when high-lying contributions or couplings are negligible. The first-order perturbation treatment of the cross-sections describes the interaction between the electromagnetic field and a system of nuclear charges. This approach has yielded reasonable estimates of the excitation amplitudes and cross sections for nuclei with final state, |f⟩, which are strongly coupled to the initial state, |i⟩ through a large matrix element, and the |f⟩ state is not strongly coupled by its diagonal matrix element or any other high-lying states.

In the subchapter 2.5, the probability equation between the ground state |i⟩ and to the final state |f⟩ was determinate in equation (2.27). If this probability P_{if} for a single encounter is much less than one, then the explicit expressions for these transition amplitudes can be obtained using first-order time-dependent perturbation theory **[6]**.

If the nucleus which undergoes the Coulomb excitation is in its ground state |i⟩ at $t \to -\infty$ the time-dependent transition amplitudes at first-order results,

$$b_{if}^{(1)} = \frac{1}{i\hbar} \int_a^b \langle f|H_{int}(t)|i\rangle e^{(i/\hbar)\,\Delta E\,t} dt,$$
(2.30)

where $H_{int}(t)$ is the monopole-multipole time-dependent interaction energy and ΔE is the excitation energy for a transition going from an initial state with energy E_i to a final state with energy E_f.

The Coulomb energy responsible for an electric multipole transition of order λ is given as **[4]**,

$$H_{int}(t) = 4\pi Z_1 e \sum_{\lambda=1}^{\infty} \sum_{\mu=-\lambda}^{\lambda} \frac{(-1)^{\mu}}{2\lambda+1} M(E\lambda, \mu) Y_{\lambda\mu}(\theta, \phi) \mathbf{r}^{-\lambda-1} \qquad (2.31)$$

where λ and μ are the multipole order of the excitation and its corresponding magnetic quantum number respectively, and $M(E\lambda, \mu)$ is the electric multipole operator, defined as,

$$M(E\lambda, \mu) = \int r^{\lambda} Y_{\lambda\mu}(\theta, \varphi) \rho(r) dr, \qquad (2.32)$$

being $\rho(r)$ the nuclear charge density and $Y_{\lambda\mu}(\theta, \varphi)$ represents the spherical harmonics.

By substituting equation (2.31) into equation (2.30) and taken into account again that if the transition probabilities are small, the transition amplitude b_{if} can be obtain as a function of the time-dependent orbital integral $S_{\mu\lambda}$, where nuclear states are labelled by I and M the total angular momentum and magnetic quantum numbers, respectively:

$$b_{if} = \frac{4\pi Z_1 e}{i\hbar} (-1)^{\mu} S_{\mu\lambda} \langle I_i M_i | M(E\lambda, \mu) | I_f M_f \rangle, \qquad (2.33)$$

$$S_{\mu\lambda} = \int_{-\infty}^{\infty} e^{(i/\hbar)\,\Delta E\cdot t} Y_{\lambda\mu}(\theta(t), \phi(r)) \mathbf{r}(t)^{-\lambda-1} dt. \qquad (2.34)$$

The multipole moment operators $M_{\lambda\mu}$ are irreducible tensors of rank λ, which therefore form a set of operators: $M_{\lambda\mu}(\lambda, \ \lambda-1, \lambda-2, \dots, -\lambda)$, and their matrix

21

elements for nuclear states I_i and I_f, can be expressed using the Wigner-Eckart theorem,

$$\langle I_i M_i | M(E\lambda, \mu) | I_f M_f \rangle = (-1)^{I_i - M_i} \begin{pmatrix} I_i & \lambda & I_f \\ -M_i & \mu & M_f \end{pmatrix} \langle I_i || M(E\lambda) || I_f \rangle \quad . \tag{2.35}$$

The final term of the equation (2.35) is a reduced (double bar) matrix and the 3-j symbol is related to a corresponding Clebsh-Gordon coefficient. The quantity Q, frequently termed the spectroscopic quadrupole moment or the static quadrupole moment, represents the diagonal element of the spherical electric quadrupole tensor, given by the next equation (2.36).

$$eQ = \left(\frac{16\pi}{5}\right)^{1/2} \frac{1}{\sqrt{2I+1}} \langle II20|II\rangle\langle I||M(E2; \mu = 0)||I\rangle \,. \tag{2.36}$$

By averaging and talking a summation over the initial and final quantum numbers of the spherical tensor in equation (2.35), it is possible to obtain an expression for the total transition rate, involving the reduced transition probability:

$$B\left(E2; I_i \to I_f\right) = \sum_{\mu M_f} |\langle I_f M_f | M(E2; \mu) | I_i M_i \rangle|^2 \,. \tag{2.37}$$

The previous equation can be expressed for a couple of nuclear states giving of the reduced transitional matrix elements according with the next equation (2.38):

$$B\left(E2; I_i \to I_f\right) = \frac{1}{2I_i+1} |\langle I_f M_f | M(E2; \mu) | I_i M_i \rangle|^2. \tag{2.38}$$

To conclude, with the previous equation (2.36), the Coulomb-excitation cross section for electromagnetic excitation may be expressed by:

22

$$\sigma_{E\lambda}^{(1)} = \left(\frac{Z_1 e}{\hbar \upsilon}\right)^2 a^{-2\lambda+2} B(E\lambda) f_{E\lambda}(\xi),$$ (2.39)

where λ represents the multipole order of the excitation. The values for the function $f_{E\lambda}(\xi)$ are tabulated in Ref. **[6]**. At small υ/c values, magnetic contributions to the total cross-sections are suppressed compared to electric excitations (Eλ) by a factor of β^2 and are, therefore, neglected in the perturbation treatment. If the excitation amplitudes are large enough, it is possible to excite nuclear states through a multiple-step process as shown in Fig 6. Under this condition, the excitation process deviates from first-order perturbation theory. Such deviations are corrected by extending the theory to second-order effects and using coupled-channel calculations.

2.5.2   Second-Order Perturbation Treatment

In the first-order perturbation theory, the excitation probability P_{if}, in a single encounter is less than unity, making the use of semi-classical approximation justifiable. However, in heavy-ion Coulomb excitation, the collision of the projectile and the target can induce a two-step excitation or excitation of multiple nuclear states which are unreachable in a single-step first order perturbation theory. At this stage the P_{if} value may be equal or exceed unity. This excitation process can be described through the second-order perturbation theory. Here, a second (final) excited nuclear state |f$_i$⟩ may be reached through excitation of an intermediate (first) state |Z$_i$⟩, from the ground state |i$_i$⟩ followed by a transition from the intermediate state to the final excited state. The final excited state |f$_i$⟩ may not be a third nuclear state lying at some energy ΔE above the intermediate state, it may arise from the excitation of the magnetic substates M_z of the first intermediate state |Z$_i$⟩ as shown in Fig 6. This process is widely known as the reorientation effect because the magnetic substates rearrange themselves depending on the shape of the nucleus.

23
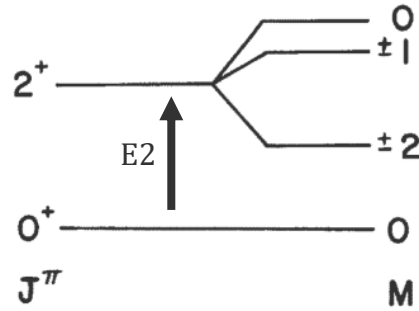
Figure 6: The reorientation effect showing the energy splitting of the magnetic substates for a
$J^\pi = 2^+$ state in a prolate even-even nucleus.

Figure 6 shows a schematic of the reorientation effect, in which the nucleus undergoing the excitation process is excited from the 0^+ ground state through E2 transition to the final 2^+ state. The probability for the Coulomb excitation in figure 6 is proportional to the reduced transition probability for an electric transition of multipole order 2. The reorientation effect for the 2^+ state causes the splitting of the magnetic substates. In this case the probability for the Coulomb excitation is also proportional, in second order, to $Q_s(2^+)$.

Continuing with the second-order perturbation theory, it is possible to say that the projectile motion may again be described by the semi-classical approximation. By calling $b_{if}^{(1)}$ and $b_{izf}^{(1,2)}$, the first-order and second-order amplitude terms, respectively, the excitation amplitudes for this second-order treatment can be written as:

$$b_{if}^{(2)} = b_{if}^{(1)} + b_{izf}^{(1,2)}.$$

(2.40)

In the previous equation (2.40), $b_{if}^{(1)}$ represents the transition from the ground state to the intermediate state, while $b_{izf}^{(1,2)}$ represents the amplitude for the transition from the intermediate state to the final state given by:

$$b_{izf}^{(1,2)} = (i\hbar)^{-2} \int_{-\infty}^{\infty} dt \langle f|H_{int}(t)|z\rangle e^{-\frac{E_f - E_z}{i\hbar}t} \int_{-\infty}^{t} dt' \langle z|H_{int}(t)|i\rangle e^{-\frac{E_z - E_i}{i\hbar}t'}.$$ (2.41)

The excitation probability P from equation (2.41), is composed of the term $P^{(1)}$, which accounts for the first-order probability, an interference term $P^{(1,2)}$ between the first order and the second-order, and a term $P^{(2)}$ which contains only second-order amplitudes. The term $P^{(1,2)}$ of the excitation probability P, would be only considered if the $P^{(2)}$ term is taken into consideration.

$$P = P^{(1)} + P^{(1,2)} + P^{(2)}. \qquad (2.42)$$

Being obtained the excitation probability, the total second-order differential cross-section may be written as:

$$d\sigma = d\sigma^{(1)} + d\sigma^{(1,2)} + d\sigma^{(2)}, \qquad (2.43)$$

$d\sigma^{(1)}$, $d\sigma^{(1,2)}$ and $d\sigma^{(2)}$ represent the first-order differential excitation cross-section, the interference between first- and second-order excitations, and the second-order differential excitation cross section, respectively.

2.6   Coulomb excitation analysis: GOSIA

The first semi-classical multiple Coulomb excitation analysis computer program, COULEX, was developed by Winther and de Boer [14] and played a vital role in the early analysis of Coulomb excitation experiments. This first code uses a set of assumed initial matrix elements, level scheme and experimental details to calculate integrated γ-ray yields, which can be compared to the experimentally measured yields.

The experiment-oriented program, GOSIA, modelled on the 1978 version [16] of COULEX has the primary purpose to design and analyse experiments and fit matrix elements. It has been extensively used in the analysis of the Coulomb-excitation measurements described in this thesis. The GOSIA code extended the Winther and de Boer code to include not only the observed γ-ray yields, but also the branching ratios between states, lifetime of the states, the *E2/M1* multipole mixing ratios and reduced matrix elements of multi-polarities, λ = 1, 2, 3, 4, 5, 6 for electric transitions and *M1* magnetic transitions only. The information

25

provided by the user enables GOSIA to locate a fit that converges to the minimum χ^2 value defined in equation (2.47). The χ^2 value is calculated using the difference between model calculation and experiment results.

The goal of this work is to extract diagonal matrix elements through the evaluation of excitation probabilities and γ-ray decay yields for a given set of matrix elements in the level scheme of argon-36. The code GOSIA will be used for data analysis. Although GOSIA is primarily used to calculate the magnitude of experimental observables, either for designing of experiments or for analysis of experimental data, experimentally inferred reduced matrix elements can also be compared to theoretical calculations in accordance with the rotational model formalism outlined by Bohr and Mottelson [17].

For a full overview of this GOSIA code, it is advised to refer to GOSIA user manual [15]. In the summary for the working of the GOSIA code, it uses two initial input data. The first one, uses the previously known information (such as reduced matrix elements and quadrupole moment) to generate theoretical matrix elements in accordance with the geometrical rotor model [18]. The second input data, contains all known parameters of the experiment, whether for target, projectile, detectors, configuration, environment or its results. With all these data set, GOSIA code compares both files to get the matrix elements data by optimizing the χ^2 parameter.

For one experiment, GOSIA calculates the Y_{exp}, Y_{point} and Y_{int} according:

$$Y_{exp}^c(I_i \rightarrow I_f) = Y_{exp}(I_i \rightarrow I_f)\frac{Y_{point}(I_i \rightarrow I_f)}{Y_{int}(I_i \rightarrow I_f)} \quad , \tag{2.44}$$

$$Y_{point}(I_i \rightarrow I_f) = sin\theta_p \int_{\phi_p} \frac{d^2\sigma(I_i \rightarrow I_f)}{d\Omega_\gamma d\Omega_p} d\phi_p \quad , \tag{2.45}$$

$$Y_{int}(I_i \rightarrow I_f) = \int_{E_{min}}^{E_{max}} dE \frac{1}{\left(\frac{dE}{dx}\right)} \int_{\theta_{p,min}}^{\theta_{p,max}} Y_{point}(I_i \rightarrow I_f) d\theta_p \quad , \quad (2.46)$$

where Y_{exp} is the experimentally measured integrated γ-ray yields. The full integration yields Y_{int} and the point yields Y_{point} are calculated in order to compare the values of Y_{exp} and its errors to get its optimal value.

The fitting of the matrix elements if performed by locating a χ^2 minimum in equation (2.47) of the experimental (actual) yields and the corrected yields,

$$\chi^2 = \frac{1}{N} \sum_i \left(\frac{Y_{exp}(i) - Y_{exp}^c(i)}{\Delta Y_{exp}(i)} \right)^2 , \quad (2.47)$$

where $Y_{exp}(i)$, $\Delta Y_{exp}(i)$ and N represent the actual yields, error and number of data points (experiments), respectively.

Once GOSIA calculates the possible approximation and its errors, the user may vary the matrix elements until the best χ^2 value is obtained **[15]** and the errors are minimized.
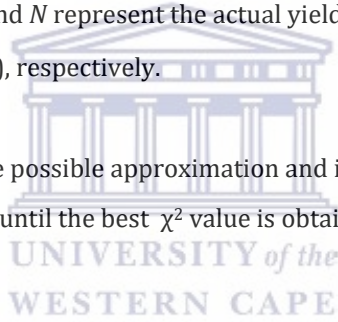
3 Coulomb Excitation Experiment

This experiment was carried out from 24th April to 28th May at iThemba LABS (Laboratory for Accelerator Based Science) in Cape Town (South Africa). The equipment used was mainly composed of beam generator, chamber, gamma and particle detectors and a data acquisitions system. Throughout chapter 3, the facility and associated equipment for measuring Coulomb excitation experiment will be discussed.

3.1 Facilities

iThemba LABS is one of the most important accelerator facilities in the African continent with the largest cyclotron in the Southern Hemisphere. It is located in Somerset West (Western Cape, South Africa) at about 50 kilometres from Cape Town city. This is a national facility of the National Research Foundation (NRF) **[19]**.

The activities at iThemba LABS are based around a number of subatomic particle accelerators. The largest of these, a K-200 is a separated sector cyclotron, that accelerates protons to energies up to 200MeV, and heavier particles to much higher energies. Smaller accelerators at iThemba LABS include the new tandetron and two injector cyclotrons, one providing intense beams of light ions, and the other, beams of polarized light ions or heavy ions.

Figure 7: iThemba LABS Facility.

iThemba LABS brings together scientists working in the physical, medical and biological sciences. The facilities provide opportunities for modern research, advanced education and the production of unique radioisotopes.

The laboratory commands a proud history for training South African and international students in a variety of research fields, including sub-atomic physics, material sciences and nuclear medicine. As a research platform of the NRF, iThemba LABS is well positioned to offer training in these areas as the researchers and users of the research facilities have professional competence to supervise postgraduate students on Honours, MSc and PhD projects. Consequentially, the supervised students are afforded hands-on opportunities for experiential training using the world class facilities on site or at partner laboratories around the world.

For more information it is advice visit the iThemba LABS website at: http://tlabs.ac.za

3.2   Equipment

3.2.1   Cyclotron Accelerator

For getting the beams according the requirement of the experiment, iThemba LABS have a series of beam lines with cyclotrons, magnets and separators. Initially, the beam ions are created in the ion source (ERC) and they are pre-accelerated with two solid-pole injector cyclotrons (SPC1 and SPC2). After that, the pre-accelerated beams are sent to the main accelerator called separated sector cyclotron (SSC). By using beam lines and magnets, the accelerated beams are distributed to the different experiment halls to be used. In our case, the ions were sent to the F-line (AFRODITE array) where the experiment was performed. Inside the AFRODITE vault the rest of the experimental equipment such as the chamber with the target, the detectors and the data acquisition system were tested.

29
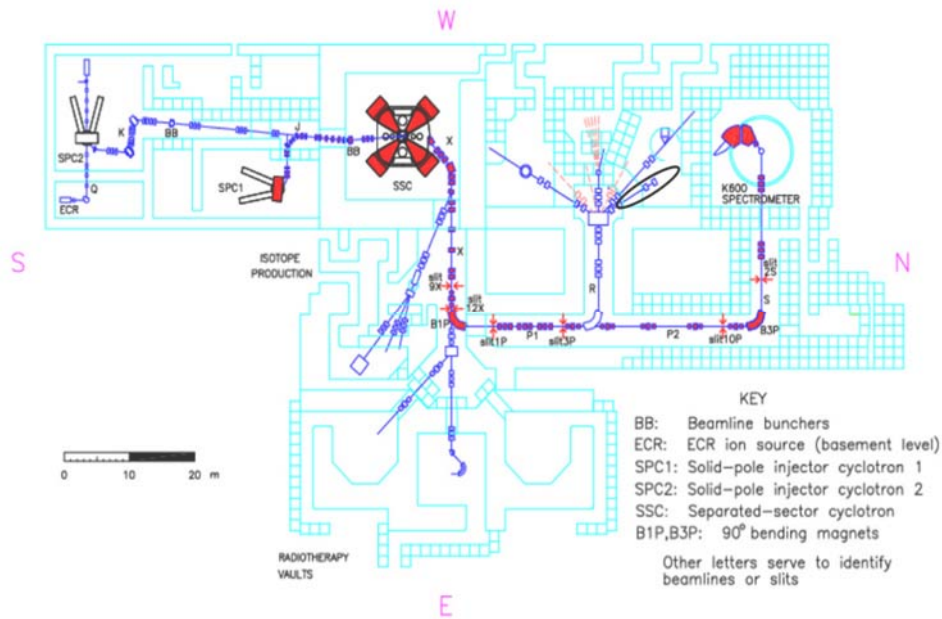
Figure 8: Floor plan distribution of the iThemba LABS facility.

3.2.2   Particle-gamma Scattering Chamber

The vacuum chamber, where the collisions between the projectile and the target nuclei take place is made of stainless steel. It has 16 square faces of the same geometry. Their walls are 2.5cm of width in order to support the extreme conditions of pressure, temperature and radiation during the experiment. It is 20cm of height and 20cm length and 20cm of width to permit setting up inside all the necessary equipment for the experiment, as target ladder, feedthrough cables, adaptor, collimator, plate shield and double-sided silicon particle detectors.
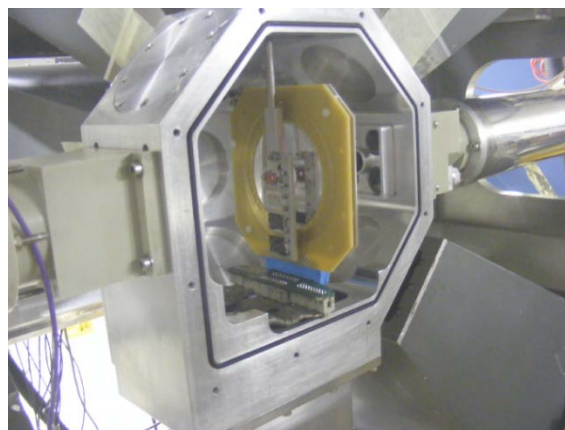
Figure 9: Scattering chamber for the ^{36}Ar Coulomb-excitation measurements.

3.2.3   Germanium Detectors (The Afrodite Array)

Outside the collision chamber there are fitted eight HPGe Clover detectors (five at 90° and three at 135°). Each Clover detector consists of four 50 x 50 x 70 mm^3 HPGe crystals housed in a cryostat. These crystals are called in this thesis a, b, c and d, and according to the distribution show on figure 10 in each clover. Crystals are closely packed in the front with a crystal-crystal distance of 0.2 mm and retains about 89% of the original crystal volume. Each crystal has a square front face with round edges. The close packing of the crystals increases the probability of detecting a Compton scattered γ-ray from the neighbouring crystal.
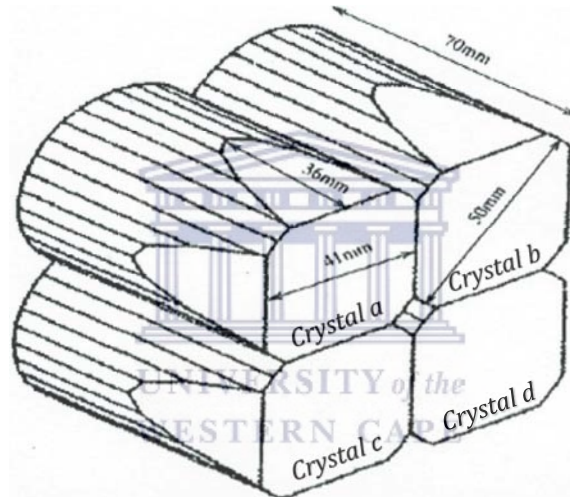
Figure 10: HPGe Clover Crystals.

Each clover is installed in conjunction with a scintillator detector and cylindrical liquid nitrogen (LN2) dewar as is possible to see in figure 11. The HPGe crystals are surrounded by a higher density scintillation detector made of bismuth germinate oxide (BGO). These are fitted with the purpose to reduce the number of partial-energy events that contributed a background event in the spectrum to analyse in the development of this thesis. Due to the very low temperature at which the detector operates, -198℃, the cylindrical liquid nitrogen LN2 dewar has been installed too.
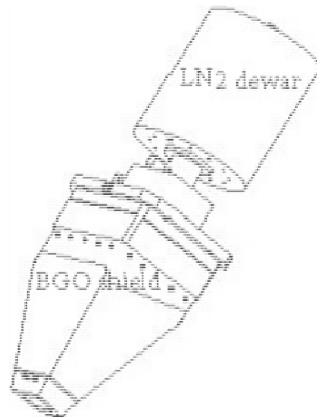
Figure 11: High Purity Germanium (HPGe) Detector.

All These eight detectors are mounted around the AFRODITE rhombicuboctahedron frame and they are placed at ϑ_{lab} of 90º and 135º with respect to the beam line (five at 90ºand three at 135º).

The AFRican Omnipurpose Detector for Innovative Techniques and Experiments array called AFRODITE array is a medium size γ-ray spectrometer array that has the unique capability of detecting both high and low energy photons with a reasonably high efficiency.
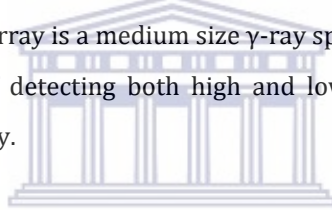
The array showed in figure 12, consists of high pure germanium detectors, their automated liquid nitrogen cooling system and the supporting electronic for signal processing connected to the system.
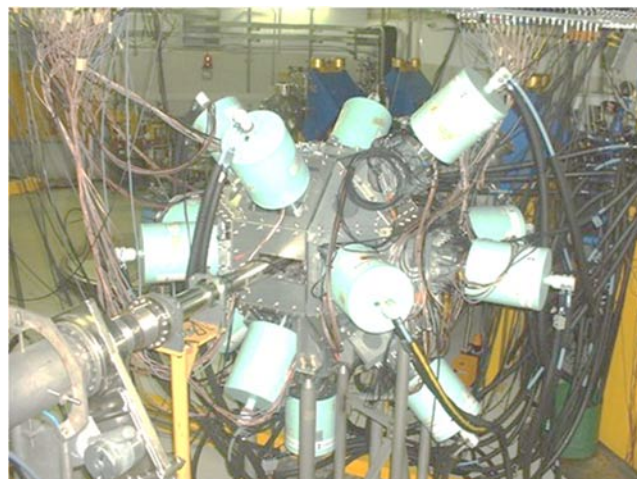
Figure 12: The Afrodite array composed of eight HPGe clover detectors.

3.2.4   S3 Silicon Detector

For detecting the scattering ions, a S3 double-sided silicon detector was installed inside the collision chamber. It was designed for Coulomb excitation studies involving radioactive ion beams [20] by Micron Semiconductors in the UK. The front face of the detector is divided in 24 rings of 886 μm in width, whereas its back side is divided in 36 sector of 11.25º. Its active detecting area goes from 22 mm and 70 mm of diameter, represented in figure 14.
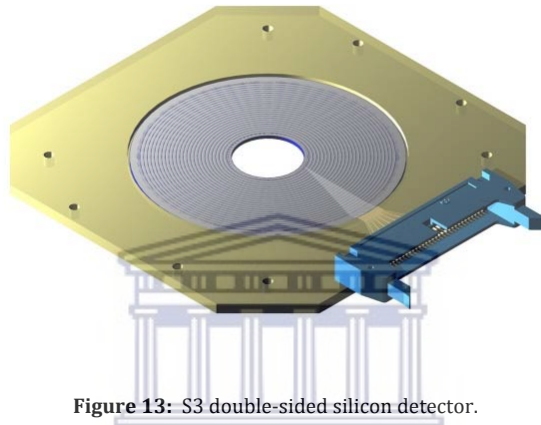
Figure 13: S3 double-sided silicon detector.
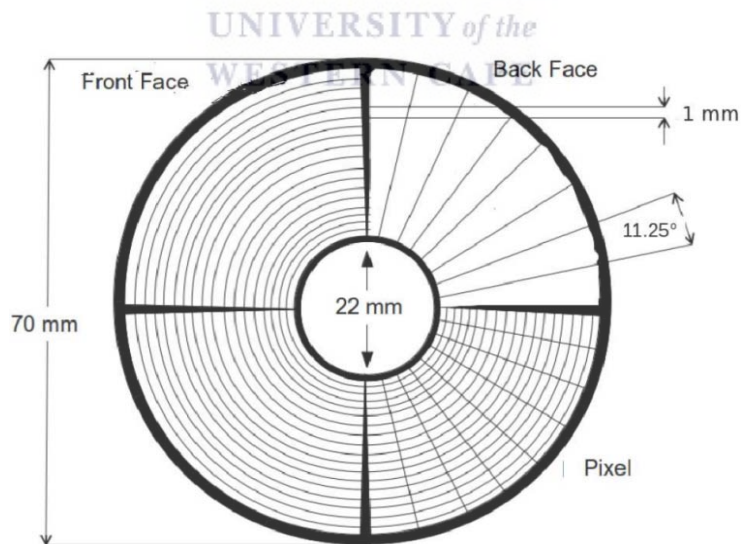
Figure 14: Schematic of the S3 double-sided silicon detector.

3.2.5 Data Acquisition

iThemba LABS facility allowed us to use a full digital data acquisition systems (DDAS) covering all the aspects of the APRODITE array. The cabling of the S3 detector shown in figure 15, was used in conjunction with the default cabling of the AFRODITE array to send the signals to a patch panel connected to the DDAS modules.

The digital data acquisition system (DDAS) used is a XIA based digital system which consists of two PXI crates. These PXI crates are capable of housing seven 16-channel Pixie-16. The first crate was loaded with two Pixie-16 modules for collection of γ signals while the second crate contained four Pixie-16 for collection of particle signals from the S3 detector. The digitized gamma and particle signals were then processed using a field-programmable gate arrays (FPGA's) to obtain energy and timing information. During the event building process, only γ-rays and particles with identical time stamps are registered. The acquired data are then sent to a PC running MIDAS (software) data acquisition system, where data is merged, filtered, build and stored.
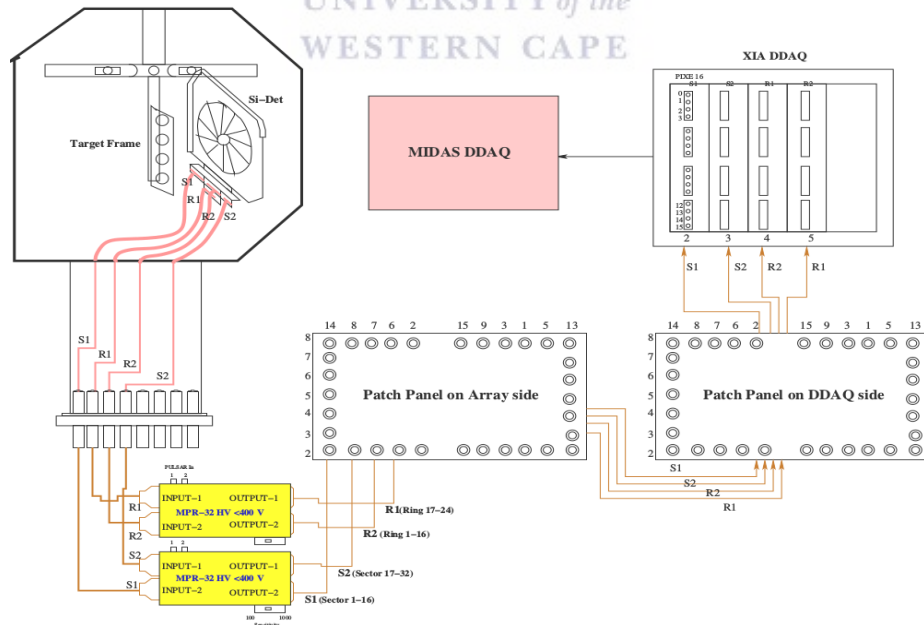
Figure 15: Electronics setup of the S3 double-sided silicon detector.

3.2.6   Software

Website: http://npg.dl.ac.uk/MIDAS/.

MIDAS (Multi Instance Data Acquisition System) it is a modular, object-based software system consisting of both the Graphical User Interface and the hardware control servers. MIDAS started as the data acquisition & electronics control software for Eurogam. Following this it has been continuously developed, taking advantage of new technologies and techniques as they have become available.

Website: https://radware.phy.ornl.gov/.

It is a software package for interactive graphical analysis of gamma-ray coincidence data. It was developed by David Radford of the Physics Division at Oak Ridge National Laboratory.

Website: http://www.srim.org/.

SRIM (The Stopping and Range of Ions in Matter) is a collection of software packages which calculate many features of the transport of ions in matter. It is a group of programs which calculate the stopping and range of ions into matter using a quantum mechanical treatment of ion-atom collisions (assuming a moving atom as an "ion", and all target atoms as "atoms"). The author is James F. Ziegler (Ph.D. Physics from Yale University, USA).

Website: http://www.pas.rochester.edu/~cline/Gosia/.

http://slcj.uw.edu.pl/en/gosia-code/.

GOSIA (Coulomb Excitation Codes) is a powerful suite of semiclassical Coulomb excitation codes developed to both design and analyse multiple Coulomb excitation experiments. These codes were originally developed at the Nuclear Structure Research Laboratory of the University of Rochester in 1980 by Tomasz Czosnyka, Douglas Cline, and Ching-Yen Wu and development has continued at Rochester, Warsaw, and Köln. The GUI RACHEL was developed by A.Hayes.

3.3   Experiment Setup

As mentioned above, the purpose of this experiment is determining the static or spectroscopic quadrupole moment Q_s of the 2_1^+ state in ^{36}Ar using the reorientation effect in Coulomb excitation. For this, a heavy ^{194}Pt target with a thickness of 1 mg/cm^2 and ^{36}Ar ions at a beam energy of 134.2 MeV were used.

A double-side S3 detector was placed upstream inside the vacuum chamber at 30mm from the center of the target position as shown in figure 16. A collimator plate was also used to prevent the beam from hitting the detector directly and an additional slit was used at the entrance of the chamber to additionally tune the beam and prevent beam haloes.
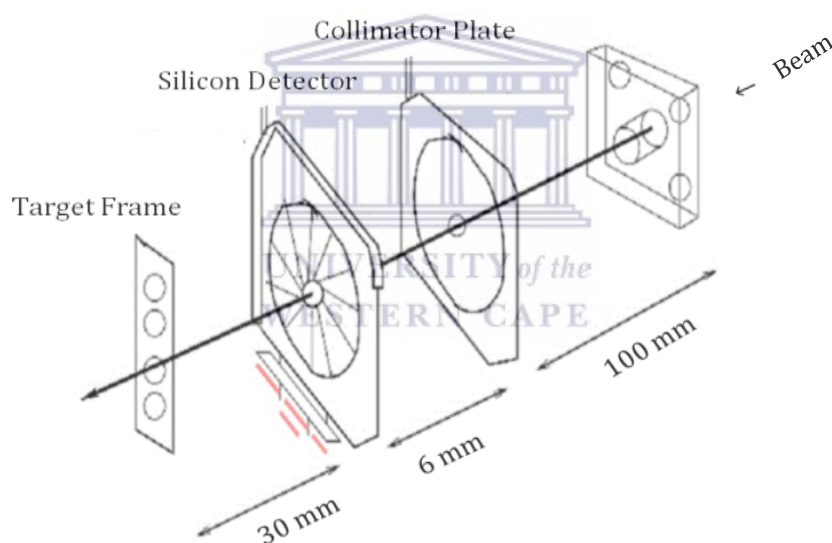
Figure 16: Configuration elements in the particle-gamma scattering chamber.

By using this distance of 30 mm, the previous experimental parameters and the geometry of the S3 detector, it was possible to obtain all data for each ring showed in table 2; where θ_{min} and θ_{max} denote the minimum and maximum scattering angles in the laboratory frame for each ring, respectively, d and dE denote the thickness of the target and average energy loss through a target of thickness d.

37

Ring#	$\theta_{min}[deg]$	$\theta_{max}[deg]$	d[mg/cm²]	dE[MeV]	$E - dE$[MeV]
1	159.06	157.60	0.75	5.04	124.53
2	157.43	156.01	0.76	5.10	124.47
3	155.85	154.46	0.77	5.16	124.40
4	154.30	152.94	0.78	5.23	124.34
5	152.79	151.47	0.79	5.30	124.27
6	151.32	150.04	0.80	5.37	124.19
7	149.89	148.64	0.81	5.45	124.12
8	148.50	147.29	0.82	5.53	124.04
9	147.15	145.98	0.83	5.61	123.95
10	145.84	144.70	0.85	5.70	123.87
11	144.57	143.47	0.86	5.78	123.78
12	143.34	142.27	0.87	5.88	123.69
13	142.15	141.11	0.89	5.97	123.59
14	140.99	139.99	0.90	6.07	123.50
15	139.88	138.90	0.92	6.17	123.40
16	138.79	137.85	0.93	6.27	123.29
17	137.74	136.83	0.95	6.37	123.19
18	136.73	135.84	0.96	6.48	123.09
19	135.75	134.89	0.98	6.58	122.98
20	134.80	133.97	0.99	6.69	122.87
21	133.88	133.08	1.01	6.80	122.76
22	132.99	132.21	1.03	6.92	122.65
23	132.13	131.38	1.04	7.03	122.53
24	131.29	130.57	1.06	7.15	122.42

Table 2: Rings, minimum and maximum scattering angles, thickness and energy loss of each ring.

The [194]Pt target was placed in the center of the chamber, thus the distance between the center of the target chamber and the front face of each clover detector remain as 19.6 cm. The clovers were fitted around the chamber according to the angles showed in table 3, where the angles θ and φ are the scattering angles in spherical coordinates from the center of the each clover.

Clover	$\theta(deg)$	$\varphi(deg)$
1	90	90
2	90	45
3	90	225
4	90	315
5	135	0
6	135	270
7	135	45
8	90	270

Table 3: Geometry of the clover detectors composing the AFRODITE array.

Using equations (2.10) and (2.21), the Somerfield parameter for this experiment is η = 114.5, which is much larger than 1, and permitted the use of the semi-classical approximation. From figure 17, it can be seen that the beam value used of 134.21 MeV satisfy the safe condition at every scattering angle.
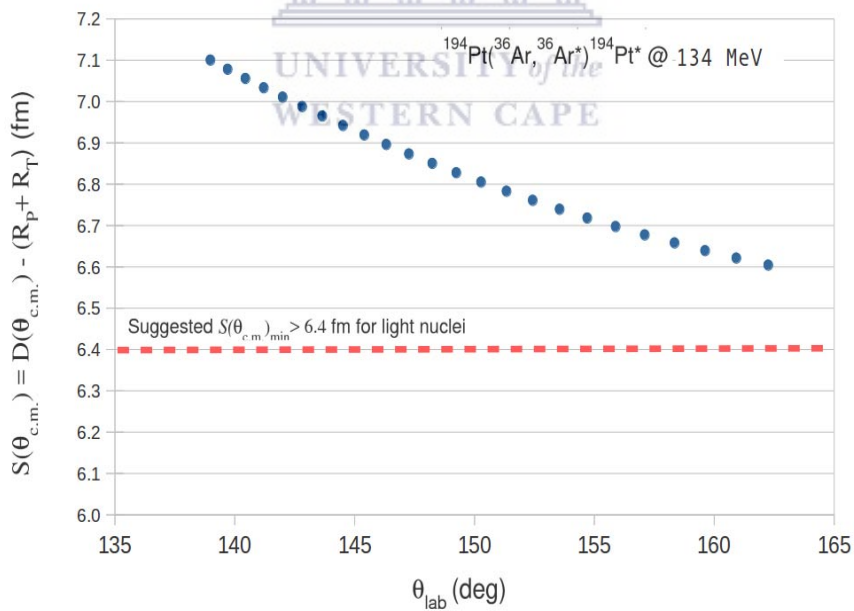
Figure 17: S(θ) at different scattering angles θ_{lab}.

4 Data Analysis

4.1 Introduction

This chapter focuses on the techniques and the methodology used for the analysis of the data obtained from this Coulomb-excitation measurement at a safe energy. The sorting of the data requires the use of the off-line sorting code MTsort from the MIDAS package, through which, once compiled, parameters can be changed; routines and subroutines can be executed and visualized in the form of ascii files and spectra for subsequent analysis. Based on previous MTsort sorting codes for particle-gamma coincidence analyses in similar experiments, a faster sorting code adapted for this particular experiment has been developed. Appendix A provides the sorting code.

4.2 Calibration

Through the MIDAS data acquisition system, the HPGe clovers and S3 silicon detectors provide events in raw spectra. The different channels are directly related to the gamma-ray energy and particle data. During the analysis it is fundamental to get a perfect calibration of the detectors in order to obtain a reliable result. Besides, in this analysis it is also necessary to compare the intensities of γ-ray peaks at different energies.

In order to perform proper energy and efficiency calibrations, radiation sources of well-known energies are required. The sources used were ^{152}Eu, ^{56}Co, ^{60}Co and ^{226}Ra. For energy calibration, these sources were placed in-front of each hemisphere of the AFRODITE array such that all the detectors can detect the emitted γ rays. For efficiency calibration the sources were placed at the target position.

4.2.1 HPGe Clover Detector

The calibration of the eight clover detectors were carried out in 4 steps. For the first and the second precalibrations were done using two different software packages, MTsort and RADWARE. Both software have the option to auto

calibrate the gamma energies by using a gamma spectrum from well-known sources. These auto calibrations are not perfect, although some results were very useful for the next calibration.

As the channels are lineally related with the gamma energies for each crystal it is possible to calculated the linear regression using the equation (E_γ=A+B*$C_{channel}$) for each crystal. Using the values obtained from the auto calibration and by looking for the high-intensity peaks from the source in the channels, it was possible to get the linear regression for each channel. Once the coefficients A and B are obtained, they were checked if they were also valid for the other less important peaks. The following example shows the calculation from linear regression for crystal *a* of the HPGE detector *1*:

WELL-KNOW Gamma Energie PEAKS   **UN-KNOW Channel PEAKS (Clover 1 Crystal a)**

ENERGY	ΔEnergy	% rel. max	Δ% rel. max	SOURCE	CHANNEL	ΔChannel	Area	ΔArea
121.78	0.002	13620	160	152Eu	181.18	0.086	5313.7	124.5
244.69	0.002	3590	60	152Eu	197.40	0.131	5065.7	158.6
295.94	0.008	211	5	152Eu	293.30	0.005	240364.7	513.9
344.28	0.004	12750	90	152Eu	594.50	0.015	47859.6	252.4
367.79	0.005	405	8	152Eu	718.84	0.169	2664.3	117.2
411.12	0.005	1070	10	152Eu	838.21	0.007	133642.7	376.8
443.98	0.005	1480	20	152Eu	895.59	0.094	4057.0	106.3
488.66	0.039	195	2	152Eu	1001.09	0.039	9706.0	126.4
564.02	0.008	236	5	152Eu	1082.40	0.031	13155.8	136.6
586.29	0.006	220	5	152Eu	1376.12	0.145	2060.0	82.8
678.58	0.003	221	4	152Eu	1656.63	0.182	1643.7	78.2
688.68	0.006	400	8	152Eu	1680.69	0.113	2684.3	84.2
778.90	0.006	6190	80	152Eu	1901.33	0.015	36065.7	200.2
867.39	0.008	1990	40	152Eu	2117.43	0.033	10910.6	120.8
964.13	0.009	6920	90	152Eu	2353.65	0.016	34932.4	196.3
1005.28	0.017	310	7	152Eu	2454.77	0.119	1751.6	61.9
1089.70	0.015	820	10	152Eu	2651.61	0.021	22483.8	160.1
1109.18	0.012	88	2	152Eu	2662.83	0.057	4454.5	79.3
1112.12	0.017	6490	90	152Eu	2715.94	0.017	29282.9	179.6
1212.95	0.012	670	8	152Eu	2865.00	0.025	15413.0	132.7
1299.12	0.012	780	10	152Eu	2962.64	0.072	2696.4	62.1
1408.01	0.014	10000	30	152Eu	3173.52	0.062	3196.8	62.6
1173.24	0.009	10000	30	60Co	3255.20	0.025	14202.3	122.9
1332.51	0.011	10000	30	60Co	3440.14	0.015	37356.5	198.5
846.77	0.008	100000	100	56Co	3561.02	0.121	1285.5	37.6
1037.84	0.006	14000	100	56Co	3570.55	0.072	2028.7	45.9
1175.10	0.006	2280	20	56Co				
1238.28	0.007	67600	400	56Co				
1360.22	0.012	4330	40	56Co				
1771.35	0.016	15700	150	56Co				
2015.18	0.016	3080	30	56Co				
2034.76	0.015	7890	70	56Co				

Table 4: Calibration data for crystal *a* of clover *1*.
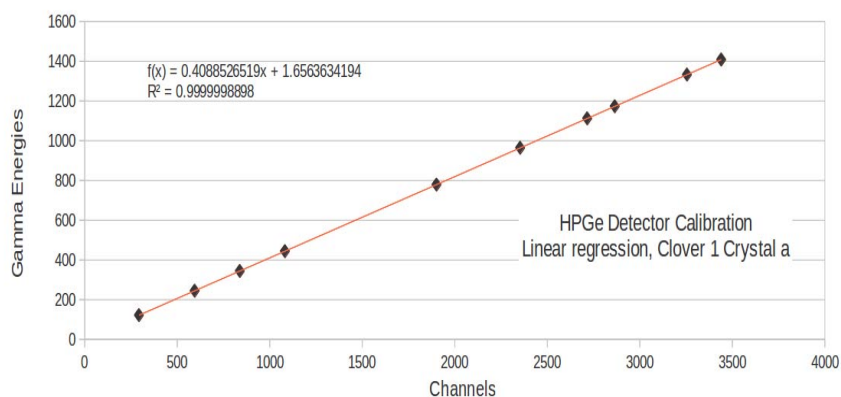
Figure 18: Linear regression for crystal *a* of clover *1*.

Once all crystals are calibrated, the spectrum should have the correct energies, giving the different gamma energies generated during the experiment.

Although the calibration with the sources can be correct, it is possible to improve it by using the well-known gamma-ray energies in the target used in the experiment as a final recalibration, and is shown in the following figures 19, 20. That is, in view of the presence of double peaks in the spectrums obtained, it forced to make a small readjust in the calibration. The procedure used for this adjustment is the same as the one discussed previously, using the sources, but this time the goal was to obtain simple peaks for all the well-known gamma-ray energies in the target (^{194}Pt).
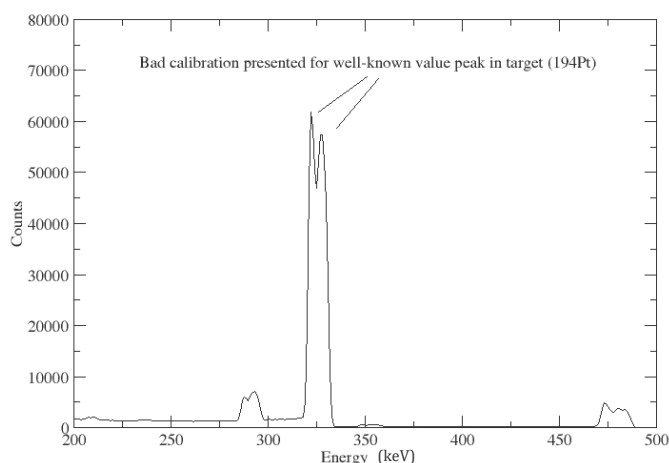
Figure 19: Bad calibration (double peak) for the well-known 328 keV peak in ^{194}Pt.

42
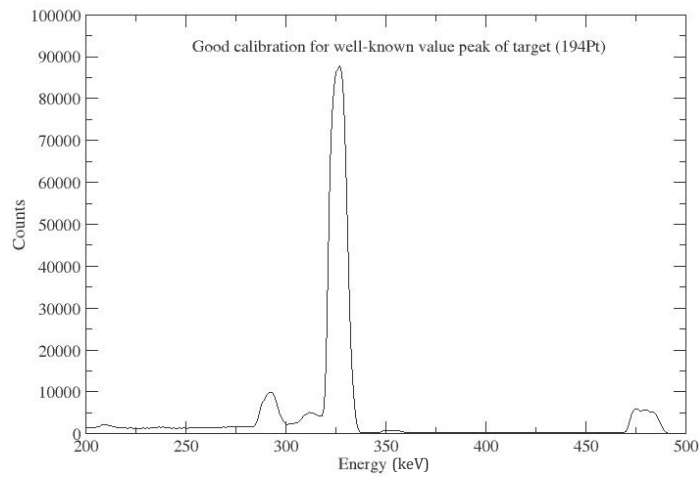
Figure 20: Good calibration in well-known gamma energy 328 keV in ^{194}Pt.

Once the manual calibration is done properly, the correct gain and offset coefficients for the linear regression of each crystal were obtained. Those values were used as an input to an off-line sorting code that generates the calibrated spectra.
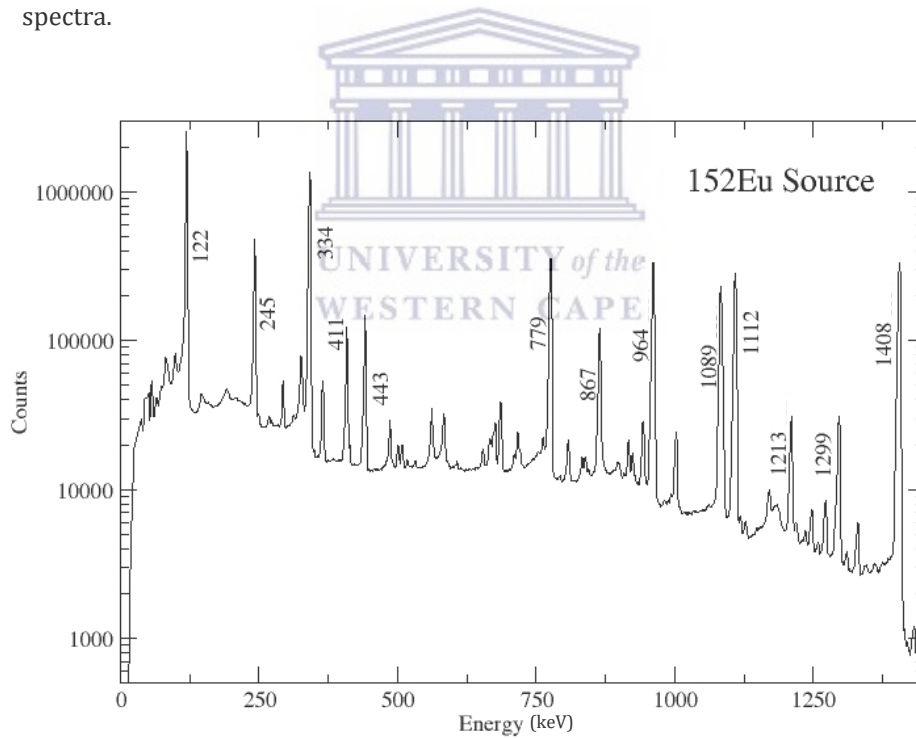
Figure 21: ^{152}Eu source spectrum used for energy and efficiency calibration.

43
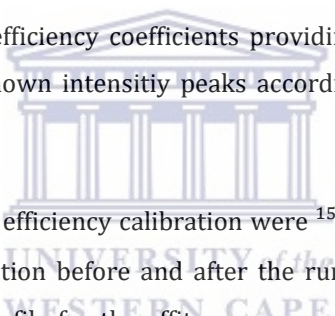
4.2.2   S3 Silicon Detector

An S3 CD-type detector was used to detect scattered particles. It is a double-sided micro-strip detector, consisting of 24 rings and 32 sectors. The calibrations for each of these rings and sectors were carried out using a two point calibration where one peak of a ^{226}Ra α-radiation source (7.8 MeV) was used in conjunction with elastic peaks simulated using GEANT4. The resulting gain and offset coefficients obtained were used in a MT-sort offline sorting code of MIDAS [21] to generate the calibrated particle energy spectra.

4.2.3   Efficiency Calibration

For the efficiency calibration, a function was used in the Radware software [22], which uses a gf3 executable file with effit as an associate program. This program is able to calculate the efficiency coefficients providing the data of calibrated peaks and theirs well-known intensitiy peaks according a special files format called *.sin.

The sources used for the efficiency calibration were ^{152}Eu and ^{56}Co, which were placed at the target position before and after the run of the experiment. The figure 22 shows the *.sin file for the effit program using ^{152}Eu as a calibration source.

AUTOCAL calibration, spectrum clovsumspecall152eucal.spe, .sou file: eu152.sou

1	119.5271	0.0005	7516642	2828	121.783	0.002	13620	160
1	242.5774	0.0016	1708180	1455	244.692	0.002	3590	60
1	341.9749	0.0011	5135754	2355	344.276	0.004	12750	90
1	408.868	0.003	389140	730	411.115	0.005	1070	10
1	441.638	0.003	518587	813	443.976	0.005	1480	20
1	584.099	0.022	68088	1178	586.294	0.006	220	5
1	776.632	0.003	1615118	1365	778.903	0.006	6190	80
1	865.13	0.004	501499	821	867.388	0.008	1990	40
1	962.005	0.0014	1627553	1366	964.131	0.009	6920	90
1	1088.769	0.012	181128	1032	1089.7	0.015	820	10
1	1110.865	0.0012	1415136	1365	1112.116	0.017	6490	90
1	1298.03	0.008	151726	441	1299.124	0.012	780	10
1	1404.6526	0.0018	1879848	1383	1408.011	0.014	10000	30

Figure 22: effit file (*.sin) for the ^{152}Eu source.

The program effit reads the data from the input files .sin and fits an efficiency curve for the data using the following expression:

$$\epsilon_\gamma = e^{\left[(A+Bx+Cx^2)^{-G}+(D+Ey+Fy^2)^{-G}\right]^{\frac{1}{G}}},$$
(4.1)

where G denotes the interaction parameter between the low and high energy region, A, B and C describe the efficiency at low energies and D, E and F describe the efficiency at high energies. The parameters x and y are given by;

$$x = log\left(\frac{E_\gamma}{100}\right),$$
(4.2)

$$y = log\left(\frac{E_\gamma}{1000}\right).$$
(4.3)

As a result of the effit program the following efficiency curve and parameters table were obtained:

$$\epsilon_\gamma = e^{\left[\left(A+B\cdot log\left(\frac{E_\gamma}{100}\right)+C\cdot log\left(\frac{E_\gamma}{100}\right)^2\right)^{-G}+\left(D+E\cdot log\left(\frac{E_\gamma}{1000}\right)+F\cdot log\left(\frac{E_\gamma}{1000}\right)^2\right)^{-G}\right]^{\frac{1}{G}}}.$$
(4.4)

A = 6.86	B = 0.7	C = 0
D = 5.44	E = -0.58	F = -0.06
G = 15		

Table 5: Fitted parameters for the efficiency calibration given in equation (4.4).

$$\eta = \exp\{ [(6.86+0.7*\ln(x/100))^{-15} + (5.445-0.584*\ln(x/1000)-0.058*\ln^2(x/1000))^{-15}]^{(-1/15)} \}$$
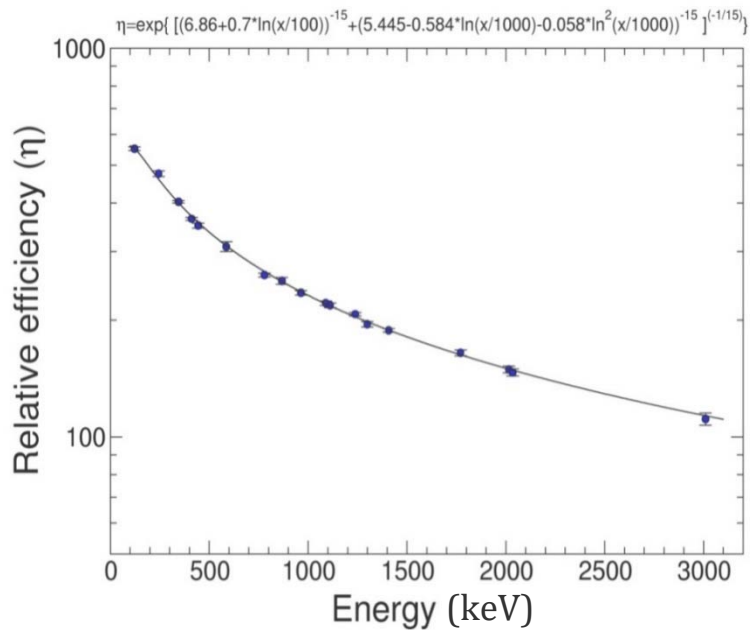
Figure 23: The [152]Eu and [56]Co sources efficiency curve from the effit RADWARE.

4.3   Background subtraction

For the correct analysis of the obtained spectra, it is very important to reduce the background as much as possible without damaging the actual valuable results. As a result of the systems used and from naturally occurring radionuclides the spectra were affected by a large and randomly distributed background. This can damage the analysis and lead to erroneous results, analysis or conclusions. For the reducing this background, the following four steps method was used.

4.3.1   Elastic energy gate condition

The off-line MTsort code considered broad elastic-peak energy gates for all rings. The condition implemented to reduce background during the sorting of the data was to require that the size of the elastic-energy gate fell between the corresponding gates for the innermost and outermost rings, as shown in figure 24.
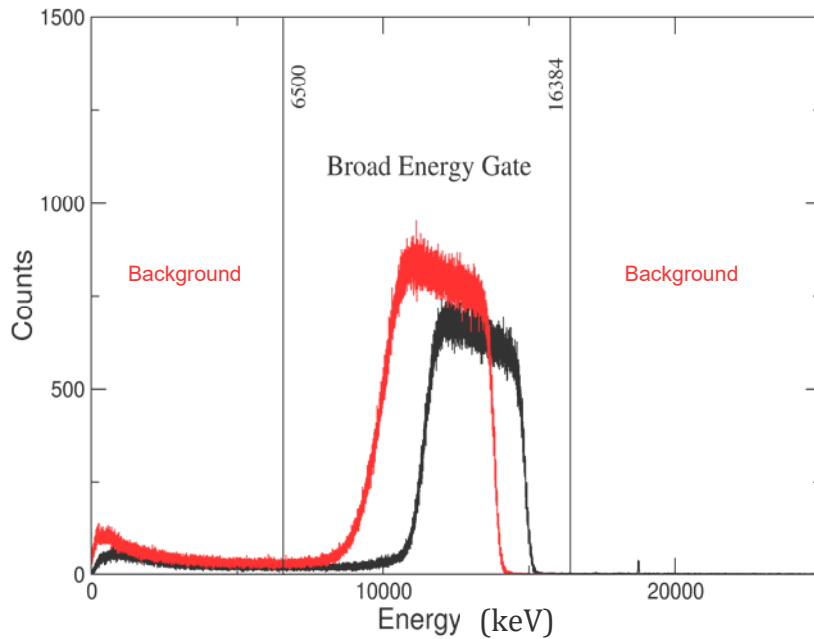
Figure 24: Elastic energy gate condition.

4.3.2 Energy sharing condition

Another source for increasing the unwanted background is when the full energy of a particle is shared between the rings, sectors (active layers) and dead layers of the S3 detector. Although the particle coincidence condition may be fulfilled, the energy detected for a double hit in the S3 detector - i.e. a simultaneous hit in a ring and a sector - can be very different. To reduce this type of unwanted background, another condition was applied for the particle energy spectra during the off-line sorting, requiring that $|E_{sector} - E_{ring}|$ were less than a given energy.

This energy condition was chosen by plotting calibrated sectors as a function of calibrated rings. This particular 2D plot is given in figure 25, which shows the diagonal line corresponding to coincidence events, while the off-diagonal events can contribute to background in the γ-ray and particle energy spectra.

47
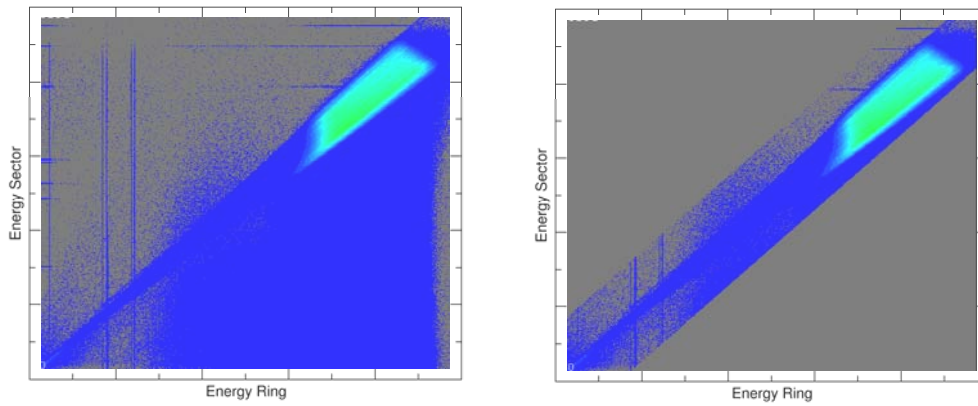
Figure 25: Energy rings Vs energy sectors before and after of share condition.

From previous experience, it is known that the implementation of this condition helps to reduce the unwanted background, particularly in the low- and medium-energy regions of the particle spectra. This tagging must be chosen as the minimum energy (maximum background removed) for which the number of counts in the 1970 keV peak of interest is conserved, i.e. the gamma ray of interest must have the same number of counts before and after applying this condition. This value was found at 2500 keV. The following figure 26 shows the counts per $\left|E_{sector} - E_{ring}\right|$ and the cutoff energy chosen.
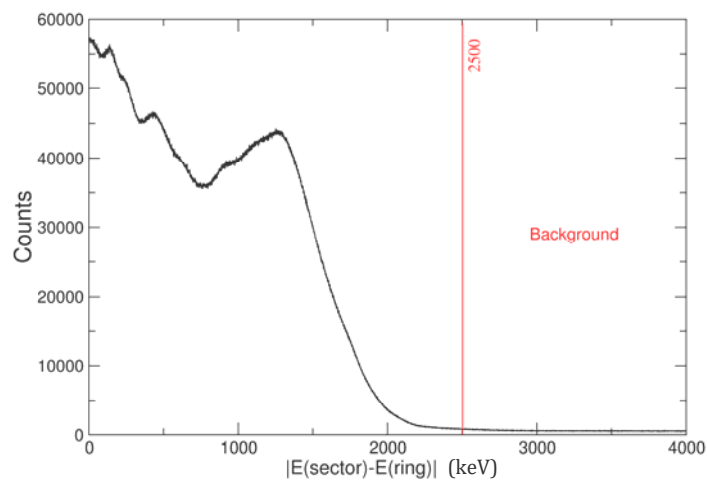
Figure 26: Counts vs $\left|E_{sector} - E_{ring}\right|$ and optimum cutoff energy.

48

4.3.3   Particle coincidence condition

From this first background reduction method, only events coming with a single hit on a ring and a single hit on the overlapping sector at the same time must be consider as an event correctly registered by the detector. A timing condition was set in the off-line sorting code by placing a time difference, Δt, acceptance gate, which measures the time difference between a hit on a ring and the subsequent hit on the adjacent sector. Figure 27 shows a small acceptable gate of Δt=160 ns, from 1015 channel to 1031 channel. This small gate represents most of the coincidence events between a ring and a sector and could give us an idea about the synchronisation quality of the data.
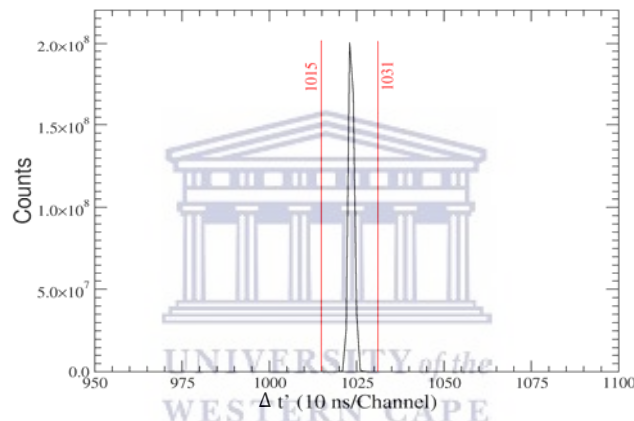
Figure 27: Particle coincidence gates.

4.3.4   Particle-Gamma coincidence condition.

In addition to the previous time coincidence required between the rings and sectors of the S3 detector, another time coincidence will have to be established between particles and gamma rays. For this purpose, further reduction of the background is done by implementing another condition of temporal coincidence between the particles detected and the simultaneous detection of a γ ray in any crystal of the clover detectors. This other condition was introduced into the off-line sorting code as another time difference, Δt, acceptance gate. All the γ rays events detected outside this time interval were considered to be background and were thus discarded. This background time gate has to have the same number of channels than the chosen prompt time gate.

49

To choose this acceptance gate we have done several sortings with different gates in order to find the optimum prompt gate, where there was a maximum number of counts in the 1970 keV of ^{36}Ar peak with a minimum number of counts of background peaks. Well-known background peaks, from typical environmental radiation in the experimental vault, were used as reference to clean the spectrum. Table 6 lists some of the typical gamma-ray peaks found as background radiation [23].

Energy (keV)	Nuclide	Energy (keV)	Nuclide
239	^{212}Pb	1120	^{214}Bi
352	^{214}Pb	1173	^{60}Co
511	β^+	1332	^{60}Co
609	^{214}Bi	1461	^{40}K
662	^{137}Cs	1765	^{214}Bi
911	^{228}Ac		

Table 6: Typical background lines in the AFRODITE vault.

Figure 28 shows the calibrated spectrum without background subtraction where it is possible to locate the previous environment gamma peaks and their importance (in counts) compared to the 1970 keV ^{36}Ar peak.
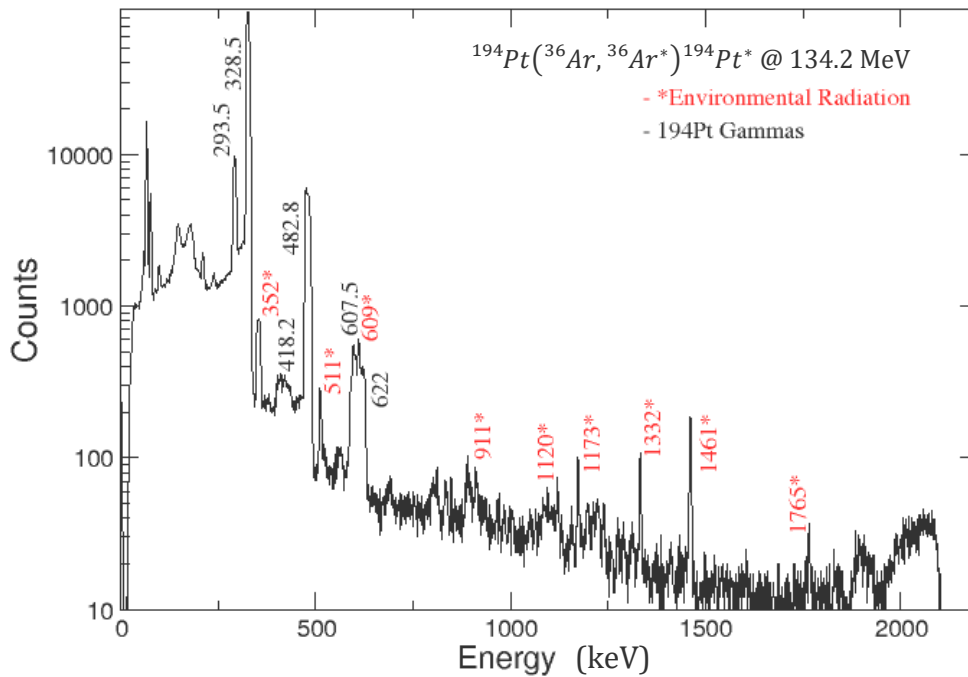
Figure 28: Non-Doppler gamma-ray energy spectrum showing peaks populated from the Coulomb-excitation reaction (black) and background (red).

An optimum prompt time gate between rings and crystals was chosen between channels 1035 and 1158, whereas the background gate was chosen from channel 889 to 1012, as shown in Figure 29. This time background subtraction was found crucial to get rid of the peaks arising from background radiation in the vault.
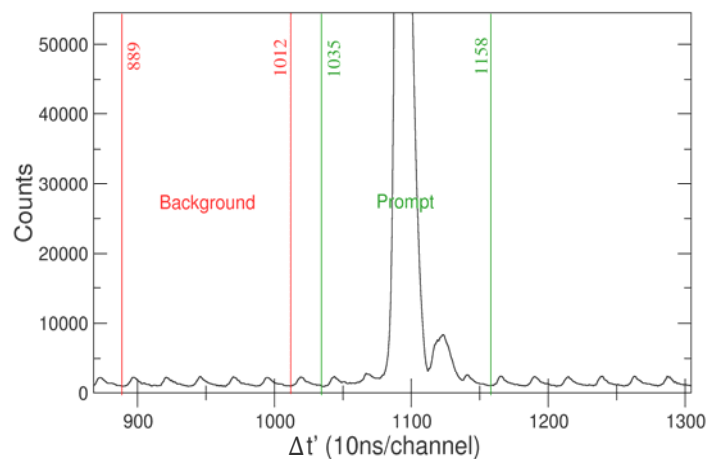
Figure 29: Time prompt (green) and background (red) gates for particle-gamma coincidences.

51
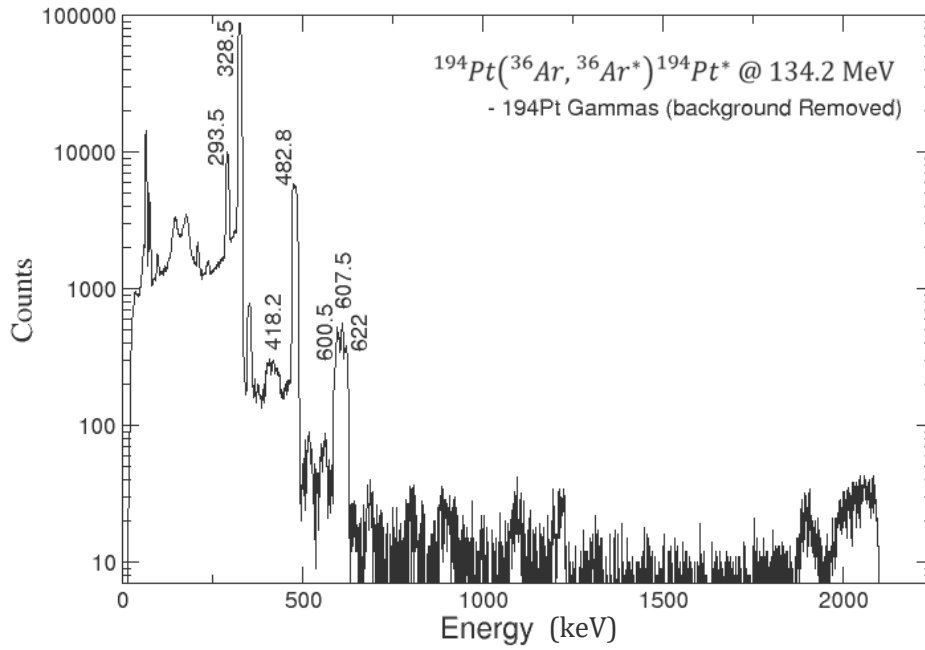
Figure 30: Non-Doppler corrected spectra with background removed.

4.4   Doppler correction

Gamma radiation emitted in-flight by the projectile traveling at a high velocity of $\beta = {}^{v}/_{c}$ - in our reaction $\beta = 0.089$ - is detected with a Doppler shift. To correct for this shift in energy of the γ rays emitted by the projectile, a Doppler correction has to be carried out to provide a clear identification of the γ ray of interest.

The Doppler correction was carried out using equation 4.5, where $\theta_{p-\gamma}$ is the angle between the trajectory of projectile and the emitted γ ray,

$$E_{\gamma,k} = \frac{E_\gamma\left(1-\beta\cos(\theta_{p-\gamma})\right)}{\sqrt{1-\beta^2}} \ . \tag{4.5}$$

To calculate $\theta_{p-\gamma}$, we used the coordinate system shown in the figure 31, where the center of the ^{194}Pt target was taken as the center of the coordinate system. Using this coordinate system, the transformation from Cartesian coordinate system to the spherical coordinate system is given by:

$$\vec{r}_{\gamma,k} = \begin{pmatrix} d_{ge}\sin\theta_k\sin\varphi_k \\ d_{ge}\cos\theta_k \\ d_{ge}\sin\theta_k\cos\varphi_k \end{pmatrix} \ . \tag{4.6}$$

52

In this transformation matrix, k denotes each clover detector from 1 to 8 and the parameter d_{ge} denotes the distance from the center of the target position to the center of each clover detector. The angles φ_γ and θ_γ for each of the crystals were calculated using the transformation matrix, and φ and θ angles from the center of the clover to the center of the crystal were considered to account for the geometric specifications of the clover, as explained in the section 3.2.3.
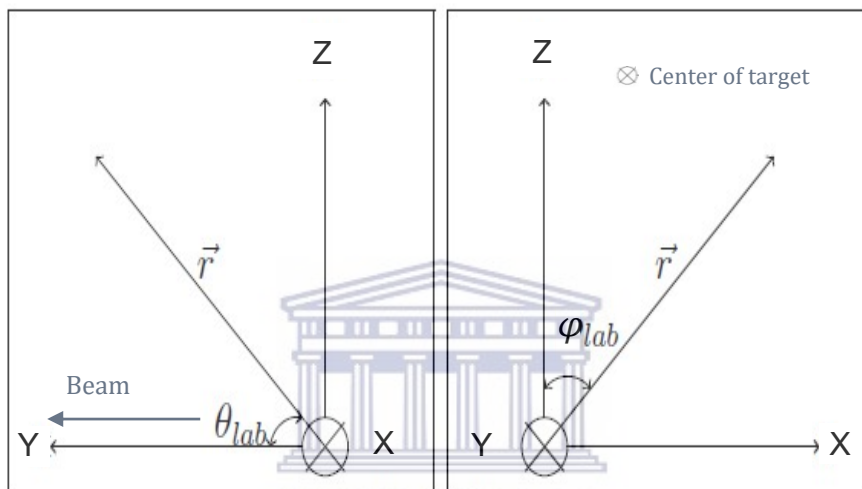
Figure 31: Coordinate system used for Doppler Correction.

Using the same coordinate system and the next transformation matrix equation (4.7), the φ and θ angles were calculated for the S3 particle detector, which coincide with the midpoints of each sector and ring, as shown in figure 31.

53
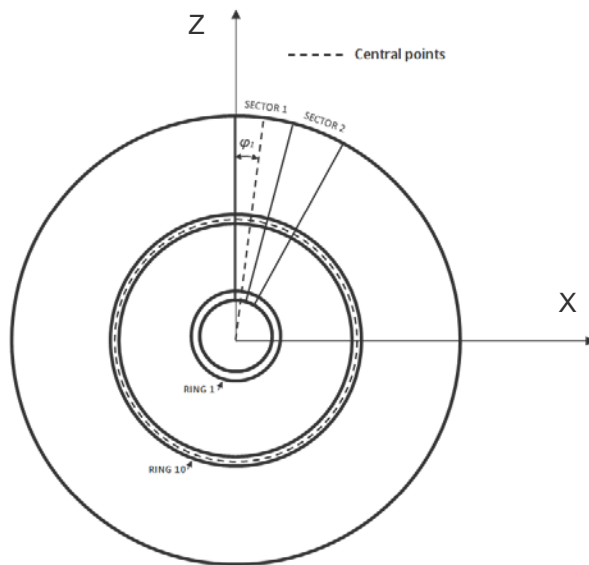
Figure 32: Rings (θ) and sectors (φ) central points for the S3 detector.

$$\vec{r}_{p,k} = \begin{pmatrix} d_r \sin\theta_k \sin\varphi_k \\ d_r \sin\theta_k \\ d_r \sin\theta_k \cos\varphi_k \end{pmatrix}. \tag{4.7}$$

In this previous transformation matrix (4.7), when one particle is detected on a ring a sector area, the parameter d_r denotes the distance from the target to the central point the ring, and the parameter k denotes the ring and sector where the particle has been detected.
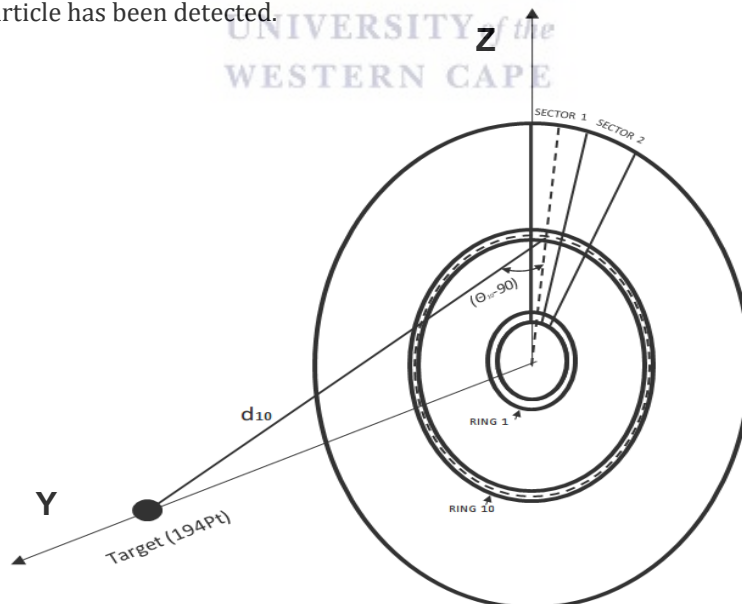
Figure 33: Distance from the target to the central point d_r of the ring.

Once the Doppler correction and all previous conditions to reduce the unwanted background have been implemented in the sorting code, it was possible to obtain a correct graphical presentation of the 1970 keV peak in ^{36}Ar, as shown in figure 34.

Figure 34 also shows the non-Doppler corrected γ-ray energy spectrum for comparison. The number of counts in the Doppler and non-Doppler corrected peaks are conserved and the area around the 1970 keV peak is clean for subsequent Coulomb-excitation analysis with the GOSIA code (see next chapter). It is encouraging to see that no background radiation from the vault is present in these spectra, which shows the power of the particle-gamma coincidence technique.
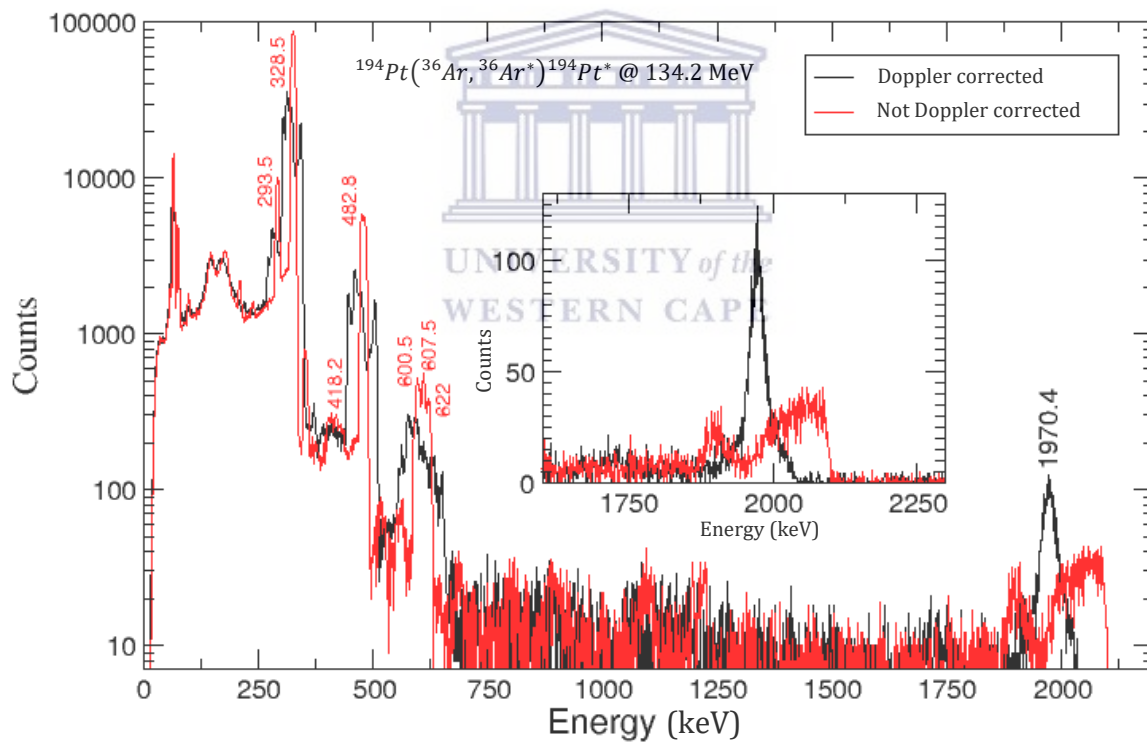
Figure 34: Doppler (black) and non-Doppler (red) corrected spectra with zoomed-in version of the high energy part.

5   GOSIA Results

The normalization procedure was applied to determine the diagonal matrix element $\langle 2_1^+ ||E2||2_1^+ \rangle$ **[24]** using the GOSIA code **[15]**. In this procedure, Coulomb-excitation curves are determined in the $\langle 2_1^+ ||E2||2_1^+ \rangle - \langle 2_1^+ ||E2||0_1^+ \rangle$ 2D plane by fixing $\langle 2_1^+ ||E2||2_1^+ \rangle$ in steps of 0.01 eb, and varying the transitional matrix element $\langle 2_1^+ ||E2||0_1^+ \rangle$ until converging with the experimentally found γ-ray intensity ratio between target and projectile, I_γ^T / I_γ^P , given by,

$$\frac{\sigma_{E2}^T W(\vartheta)^T}{\sigma_{E2}^P W(\vartheta)^P} = 1.037 \, \frac{N_\gamma^T}{N_\gamma^P} \frac{\varepsilon_\gamma^P}{\varepsilon_\gamma^T} = \frac{I_\gamma^T}{I_\gamma^P} \, , \tag{5.1}$$

where $W(\vartheta)$ represents the integrated angular distribution of the de-excited γ rays in coincidence with the inelastic scattered particles **[25]** and the factor 1.037 accounts for the 96.45% isotopic enrichment of the ^{194}Pt target chosen for normalization. The normalization of the γ-ray yield in ^{36}Ar to the well-known matrix elements in the target nucleus, ^{194}Pt, minimizes systematic effects such as dead time and pile-up rejection. Relative efficiencies of $\varepsilon_\gamma^P = 152(5)$ and $\varepsilon_\gamma^T = 409(8)$, and total counts of $N_\gamma^P = 4725(105)$ and $N_\gamma^T = 860471(961)$ for the 1970 keV and 328 keV γ–ray transitions, respectively, yield $I_\gamma^T / I_\gamma^P = 65(3)$. The quoted error on this measurement arises from the uncertainties of N_γ^P (2.2%) and ε_γ^P (3.0%).

The following table 7 shows the counts per rings for the target and projectile obtained during the experiment.

		N. Counts	
Ring	Average $\bar{\theta}$ Angle (deg)	$^{36}_{18}Ar$	$^{194}_{78}Pt$
1	158,33	133	25951
2	156,72	155	29395
3	155,15	144	31127
4	153,62	158	32562
5	152,13	202	33583
6	150,67	223	35139
7	149,26	178	36080
8	147,89	223	36248
9	146,56	211	37251
10	145,27	188	37695
11	144,02	171	37571
12	142,80	231	38219
13	141,63	205	38506
14	140,49	194	37884
15	139,38	221	38533
16	138,32	190	38557
17	137,28	223	38449
18	136,28	198	38463
19	135,32	227	37373
20	134,38	252	38126
21	133,47	198	36883
22	132,60	170	36584
23	131,75	222	36284
24	130,93	208	34008
TOTAL		**4725**	**860471**

Table 7: Number of counts per ring.

The resulting Coulomb-excitation diagonal band is shown in Figure 35, where the red dashed line is the central value and the two red solid lines correspond to the 1σ loci limits. The horizontal band represents $\langle 2^+_1||E2||0^+_1 \rangle = 0.1825(56)$ eb **[26]**. The interception of both center lines yields $Q_s(2^+_1) = +0.09(3)$ eb according to equation (2.3) given in chapter 2 ($Q_s(2^+_1) = 0.75793 \langle 2^+_1||E2||2^+_1 \rangle$), The error of $\langle 2^+_1||E2||2^+_1 \rangle$ was determined from the overlap region between the two bands assuming central values for the $\langle 2^+_1||E2||0^+_1 \rangle$ band, ±0.025 eb, and the Coulomb-excitation diagonal curve, ±0.033 eb, added in quadrature.

Assuming an ideal rotor, and according with equation (2.2), $Q_s(2^+_1) = -\frac{2}{7} Q_0$, which yields a negative value obtained for the intrinsic quadruple moment Q_0 corresponding to an oblate shape.
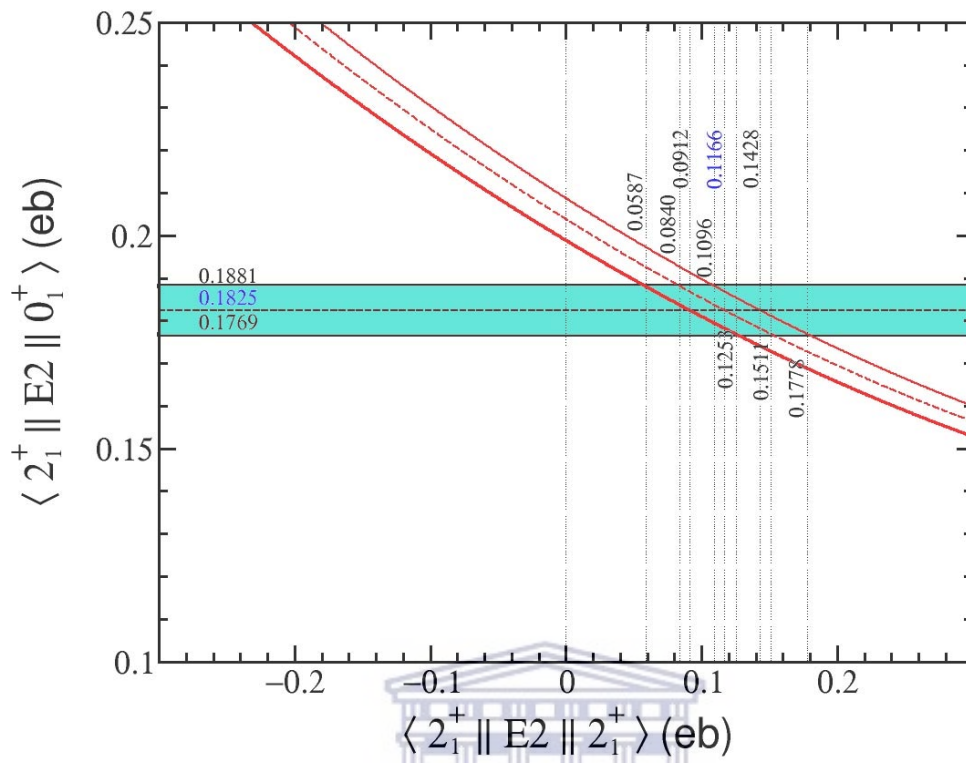
Figure 35: Variation of $\langle 2_1^+||E2||0_1^+\rangle$ as a function of $\langle 2_1^+||E2||2_1^+\rangle$ in ^{36}Ar .

6   Discussion and Conclusions

Figure 36 shows $Q_s(2_1^+)$ values determined in the sd-shell, including shell model calculations (triangle data point) and the $Q_s(2_1^+)$ values determined for ^{36}Ar through the reorientation effect carried out in this work (diamond data point) and the rotational model, i.e. through the B(E2) value from the NNDC data base **[26]** (circle data points). The $Q_s(2_1^+)$ value extracted from the rotational model can only provide the magnitude and not the sign of the spectroscopic quadrupole moment; hence, the two possible (positive and negative) values. For comparison, the $Q_s(2_1^+)$ value for ^{40}Ar is included from Elijah Akakpo's MSc work, which was also carried out during the April-May 2016 Coulomb excitation campaign at iThemba LABS.
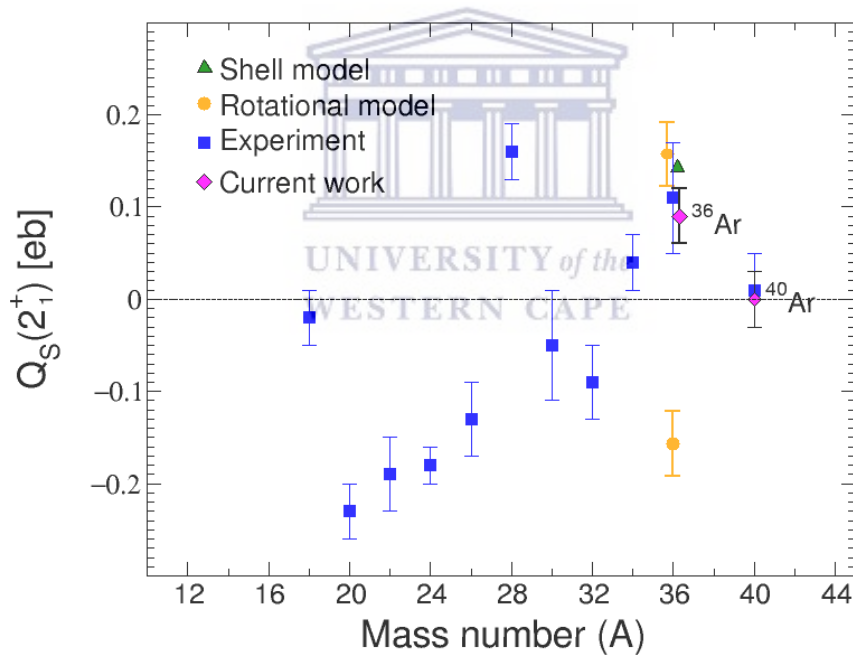
Figure 36: Experimental $Q_s(2_1^+)$ values previously determined in the sd-shell (squares) together with values determined in the Ar isotopes by our group (diamonds).

The new $Q_s(2_1^+)$ value determined for ^{36}Ar, $Q_s(2_1^+) = +0.09(3)$ eb, is more accurate than the one given in previous work. The zig-zag pattern remains, with a clearly oblate shape for the 2_1^+ state in ^{36}Ar, as suggested by the pairing coupling scheme [27]. Within this pairing model, a prolate shape is expected at the beginning of the sd shell as particles start filling up the empty shells, and similarly, there is an expected flip over to oblate shapes at around mid-shell, when it is more appropriate to talk about holes in the filled shell, which align their orbits along the polar axis, hence leading to oblate shapes. Towards the end of the shell the dominant pairing of holes again restores the spherical shape, which is what probably happens for ^{40}Ar. It is interesting to note that the $Q_s(2_1^+)$ values determined from the reorientation effect in this work and the one determined using the rotational model from the B(E2) value are in disagreement at the 1-σ confidence level. Current state-of-the-art mean-field calculations of the $Q_s(2_1^+)$ value in ^{36}Ar [28, 29] yield +0.13 eb, a value in reasonable agreement with our work, although slightly overestimated.

Finally, it is the intention of this work to motivate further state-of-the-art mean-field calculations to estimate the formation of clustering structures already present in the 2_1^+ state in ^{36}Ar, and see how this relates to the ^{36}Ar + α super-deformed band in ^{40}Ca.

Appendix A – Sorting Code.

```
*formats
clover[1:8](e1, e2, e3, e4, x1, x2, x3, x4)
sect[21:52](e1, x1)
ring[53:77](e1, x1)

*data
!#########################_CLOVER_CALIBRATION_#########################

Gainarray SegA
1 (0.656363 0.408853 0.000)
2 (2.640653 0.5572010.000)
3 (0.367806 0.389060 0.000)
4 (1.098420  0.384518 0.000)
5 (3.4125600.3746740.000)
6 (1.943800  0.3733920.000)
7 (1.527600  0.569731 0.000)
8 (-1.059450  0.368514 0.000)

Gainarray SegB
1 (1.858420  0.380868 0.000)
2 (0.209477 0.538851 0.000)
3 (2.023610  0.371267 0.000)
4 (1.0777300.393432 0.000)
5 (1.522810  0.3798370.000)
6 (4.0426400.373059 0.000)
7 (2.204630  0.541471 0.000)
8 (3.802950  0.3832640.000)

Gainarray SegC
1 (5.5383800.413871 0.000)
2 (2.616820  0.377610 0.000)
3 (0.022845 0.468353 0.000)
4 (2.023670  0.671319 0.000)
5 (0.467696 0.360091 0.000)
6 (0.000000  0.0000000.000)
7 (1.655370  0.3559870.000)
8 (1.041920  0.5900590.000)

Gainarray SegD
1 (0.671850  0.414518 0.000)
2 (1.611200  0.424141 0.000)
3 (0.421586 0.400266 0.000)
4 (1.948310  0.3766990.000)
5 (1.521440  0.3609320.000)
6 (0.506130  0.363203 0.000)
7 (0.785110  0.525142 0.000)
8 (2.786540  0.358587 0.000)

!###################_RING_AND SECTOR_CALIBRATION_####################

Gainarray ring
53 (-1238.62 49.22 0.000)
54 (-1136.89 48.970.000)
55 (-1184.42 48.65 0.000)
56 (-1349.19 48.560.000)
57 (-1171.04 47.41 0.000)
58 (-1147.37 47.560.000)
59 (-1146.20 47.41 0.000)
60 (-1129.41 47.630.000)
61 (-1095.94 46.77 0.000)
```

62 (-1080.24 45.770.000)
63 (-1093.73 45.57 0.000)
64 (-1054.00 44.650.000)
65 (-1030.86 45.02 0.000)
66 (-994.02 44.580.000)
67 (-1014.81 44.85 0.000)
68 (-996.18 44.35 0.000)
69 (-974.77 42.730.000)
70 (-970.96 42.98 0.000)
71 (-948.59 43.520.000)
72 (-940.48 43.53 0.000)
73 (-935.81 43.670.000)
74 (-917.04 42.24 0.000)
75 (-886.70 41.570.000)
76 (-917.03 42.07 0.000)
77 (0.00 0.00 0.000)

Gainarray sect
21 (-1158.93 11.86 0.000)
22 (-1156.15 11.880.000)
23 (-1179.06 12.03 0.000)
24 (-1145.97 11.890.000)
25 (-1143.83 11.75 0.000)
26 (-1140.01 11.830.000)
27 (-1131.83 11.64 0.000)
28 (-1122.52 11.970.000)
29 (-1129.56 11.55 0.000)
30 (-1120.10 11.760.000)
31 (-1118.55 11.86 0.000)
32 (-1135.51 11.730.000)
33 (-1127.39 11.88 0.000)
34 (-1137.31 11.790.000)
35 (-1148.79 11.92 0.000)
36 (-1151.68 12.240.000)
37 (-1142.35 11.67 0.000)
38 (-1158.33 11.790.000)
39 (-1167.82 11.76 0.000)
40 (-1182.28 11.850.000)
41 (-1182.11 12.10 0.000)
42 (-1188.44 11.910.000)
43 (-1195.42 12.24 0.000)
44 (-1233.50 12.31 0.000)
45 (-1198.39 11.860.000)
46 (-1195.90 12.00 0.000)
47 (-1195.19 12.300.000)
48 (-1188.25 12.23 0.000)
49 (-1210.47 11.930.000)
50 (-1176.09 11.81 0.000)
51 (-1171.85 11.650.000)
52 (0.00 0.00 0.000)

!######################_VARIABLE_DECLARATIONS_#########################

longlong tg = 0, ts = 0, tr = 0, td = 0, tga = 0, tgb = 0, tgc = 0, tgd = 0, tdr = 0, tds = 0
longlong tss1 = 0, trr1 = 0, tdgr = 0, tdgs = 0, tdddd = 0
float xa, xbb, xc, xd, xb, ya, ybb, yc, yd, yb, za, zbb, zc, zd, zb, caa, cab, cac, cad
valuearray tg1[1:8]
0 0 0 0 0 0 0 0
valuearray energyg1[1:8]
0 0 0 0 0 0 0 0
valuearray tg2[1:8]
0 0 0 0 0 0 0 0
valuearray energyg2[1:8]
0 0 0 0 0 0 0 0
valuearray tg3[1:8]

62

```
0 0 0 0 0 0 0 0
valuearray energyg3[1:8]
0 0 0 0 0 0 0 0
valuearray tg4[1:8]
0 0 0 0 0 0 0 0
valuearray energyg4[1:8]
0 0 0 0 0 0 0 0
valuearray sum[1:8]
0 0 0 0 0 0 0 0
valuearray nrr[1:24]
0 0 0 0 0 0 0 0
0 0 0 0 0 0 0 0
0 0 0 0 0 0 0 0
valuearray nss[1:32]
0 0 0 0 0 0 0 0
0 0 0 0 0 0 0 0
0 0 0 0 0 0 0 0
0 0 0 0 0 0 0 0
valuearray energyr[1:24]
0 0 0 0 0 0 0 0
0 0 0 0 0 0 0 0
0 0 0 0 0 0 0 0
valuearray energys[1:32]
0 0 0 0 0 0 0 0
0 0 0 0 0 0 0 0
0 0 0 0 0 0 0 0
0 0 0 0 0 0 0 0
valuearray tr1[1:24]
0 0 0 0 0 0 0 0
0 0 0 0 0 0 0 0
0 0 0 0 0 0 0 0
valuearray ts1[1:32]
0 0 0 0 0 0 0 0
0 0 0 0 0 0 0 0
0 0 0 0 0 0 0 0
0 0 0 0 0 0 0 0
valuearray  sumdop[1:8]
0 0 0 0 0 0 0 0
valuearray  sumdopx[1:8]
0 0 0 0 0 0 0 0
valuearray  sumnodop[1:8]
0 0 0 0 0 0 0 0
valuearray  sumnodopx[1:8]
0 0 0 0 0 0 0 0
valuearray  e11ca[1:8]
0 0 0 0 0 0 0 0
valuearray  e11cb[1:8]
0 0 0 0 0 0 0 0
valuearray  e11cc[1:8]
0 0 0 0 0 0 0 0
valuearray  e11cd[1:8]
0 0 0 0 0 0 0 0
valuearray  x_1[1:8]
0 0 0 0 0 0 0 0
valuearray  x_2[1:8]
0 0 0 0 0 0 0 0
valuearray  x_3[1:8]
0 0 0 0 0 0 0 0
valuearray  x_4[1:8]
0 0 0 0 0 0 0 0
valuearray  y_1[1:8]
0 0 0 0 0 0 0 0
valuearray  y_2[1:8]
0 0 0 0 0 0 0 0
valuearray  y_3[1:8]
```

```
0 0 0 0 0 0 0 0
valuearray  y_4[1:8]
0 0 0 0 0 0 0 0
valuearray  z_1[1:8]
0 0 0 0 0 0 0 0
valuearray  z_2[1:8]
0 0 0 0 0 0 0 0
valuearray  z_3[1:8]
0 0 0 0 0 0 0 0
valuearray  z_4[1:8]
0 0 0 0 0 0 0 0
valuearray sumdr[1:24]
0 0 0 0 0 0 0 0
0 0 0 0 0 0 0 0
0 0 0 0 0 0 0 0
valuearray sumndr[1:24]
0 0 0 0 0 0 0 0
0 0 0 0 0 0 0 0
0 0 0 0 0 0 0 0
valuearray sumdrab[1:24]
0 0 0 0 0 0 0 0
0 0 0 0 0 0 0 0
0 0 0 0 0 0 0 0
valuearray eegdop[1:9]
0 0 0 0 0 0 0 0 0
float  pi = 3.14
```

!################_DETECTOR_DISTANCES_FROM_TARGET_###################

```
float  d_target2ge = 19.60, d_target2s3 = -3.00
```

!####################_THETA_ANGLE_OF_CLOVERS_#######################

```
valuearray ge_theta[1:8]
1.57080 1.57080   1.57080   1.57080   2.35620   2.35620   2.35620   1.57080
```

!#####################_PHI_ANGLE_OF_CLOVERS_#######################

```
valuearray ge_phi[1:8]
1.57080 0.78540   3.92700   5.49779   0.00000   4.71239   0.78540   4.71239
```

!#######################_THETA_ANGLE_OF_RINGS_######################

```
valuearray angdis[1:24]
2.76330 2.73524   2.70784   2.68112   2.65509   2.62976
2.60513 2.58120   2.55796   2.53542   2.51356   2.49238
2.47185 2.45197   2.43272   2.41409   2.39605   2.37860
2.36171 2.34536   2.32955   2.31424   2.29943   2.28509
```

!###########################_BETA_#################################

```
valuearray beta[1:24]
0.06125 0.06102   0.06087   0.06081   0.06080   0.06087
0.06098 0.06113   0.06131   0.06151   0.06173   0.06196
0.06219 0.06243   0.06266   0.06290   0.06395   0.06395
0.06395 0.06395   0.06395   0.06395   0.06395   0.06395
```

!####################_PHI_ANGLE_OF_SECTORS_########################

```
valuearray sec_phi[1:32]
0.09817 0.29452   0.49087   0.68722   0.88357   1.07992   1.27627   1.47262
1.66897 1.86532   2.06167   2.25802   2.45437   2.65072   2.84707   3.04342
3.23977 3.43612   3.63247   3.82882   4.02516   4.22152   4.41786   4.61421
4.81056 5.00691   5.20326   5.39961   5.59596   5.79231   5.98866   6.18501
```

!#####################_THETA_ANGLE_OF_CRISTALS_######################

valuearray crys_a_theta[1:8]
1.48 1.48 1.48 1.48 2.27 2.27 2.27 1.48
valuearray crys_b_theta[1:8]
1.66 1.661.66 1.66 2.45 2.45 2.45 1.66
valuearray crys_d_theta[1:8]
1.66 1.66 1.66 1.66 2.45 2.45 2.45 1.66
valuearray crys_c_theta[1:8]
1.48 1.481.48 1.48 2.27 2.27 2.27 1.48

!#####################_PHI_ANGLE_OF_CRISTALS_######################

valuearray crys_a_phi[1:8]
1.66 0.87 4.02 5.59 0.09 4.80 0.87 4.80
valuearray crys_c_phi[1:8]
1.66 0.874.02 5.59 0.09 4.80 0.87 4.80
valuearray crys_b_phi[1:8]
1.48 0.69 3.84 5.41 6.19 4.62 0.69 4.62
valuearray crys_d_phi[1:8]
1.48 0.693.84 5.41 6.19 4.62 0.69 4.62

!#######################_INELASTIC_GATES_######################

valuearray inelas_max[1:24]
153441532615219 15224 15139 15094
15032 15008 14939 14953 14902 14827
14749 1475014685 14610 14586 14540
14502 1446814407 14408 14458 14325
valuearray inelas_min[1:24]
08415 08440 08358 08273 08284 08187
08154 0808408010 07966 07816 07841
07754 07682 07635 07544 07493 07406
07264 0725907217 07123 07096 07013
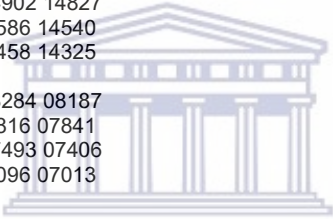
*spectra
!######################_SPECTRUM_DEFINITIONS_######################

!rclovera: gamma spectra for crystal a
!rcloverb: gamma spectra for crystal b
!rcloverc: gamma spectra for crystal c
!rcloverd: gamma spectra for crystal d
!sectors: particle energy spectra for sectors
!ring:particle energy spectra for sectors
!hitpatg: hitpattern for Ge detectors
!hitpatr: hitpattern for rings
!hitpats: hitpattern for sectors
!timesi: ring and time difference spectrum
!timeg1: ring and gamma time difference spectrum
!timeg2: sector and gamma time difference spectrum
!ge_sum_no_dopplerr: non Doppler corrected gamma spectra for individual rings and all clovers (after conditions)
!ge_sum_no_doppler: non Doppler corrected gamma spectra for all rings and all clovers (after conditions)
!ge_sum_no_dopplerr2: non Doppler corrected gamma spectra for individual rings (after conditions)
!ge_sum_no_doppler2: non Doppler corrected gamma spectra for all rings (after conditions)
!ge_sum_dopplerr: Doppler corrected gamma spectra for individual rings and all clovers (after conditions)
!ge_sum_doppler: Doppler corrected gamma spectra for all rings and all clovers (after conditions)
!ge_sum_dopplerr2: Doppler corrected gamma spectra for individual rings (after conditions)
!ge_sum_doppler2: Doppler corrected gamma spectra for all rings (after conditions)
!ge_sum_doppleraddbb[1:24]: Doppler corrected gamma spectra for each ring (after conditions)
!ge_sum_doppleraddb:add back Doppler corrected gamma spectra for all rings (after conditions)
!2D ring-gamma histogram (ring-gamma time difference (x-axis) & sum of all clover energies (y-axis))
!2D sector-gamma histogram (sector-gamma time difference (x-axis) & sum of all clover energies (y-axis))
!si_mat: 2d si matrix (sector energy (x axis) & ring energy (y axis))

rclovera[1:8] 16384

```
rcloverb[1:8] 16384
rcloverc[1:8] 16384
rcloverd[1:8] 16384
sectors[1:32] 65536
rings[1:24] 65536
hitpatg 108 32
hitpatr 108 32
hitpats 64 32
timesi 4096 32
timeg1 4096 32
timeg2 4096 32
ge_sum_no_dopplerr[1:24] 16384 32
ge_sum_no_doppler 16384 32
ge_sum_no_dopplerr2[1:24] 16384 32
ge_sum_no_doppler2 16384 32
ge_sum_dopplerr[1:24] 16384 32
ge_sum_doppler 16384 32
ge_sum_dopplerr2[1:24] 16384 32
ge_sum_doppler2 16384 32
ge_sum_doppleraddbb[1:24] 16384 32
ge_sum_doppleraddb 16384 32
matdgr  2048 2d
matdgs  2048 2d
si_mat  4096 2d
eeg 4096 32
eegdc 4096 32
si_matdc 4096 2d

*commands
!#############################_COMMANDS_#############################

doloop i from 1  to 32 step +1
{
energys(i) =  0
ts1(i) =  0
}
doloop i from 1  to 24 step +1
{
energyr(i) =  0
tr1(i) =  0
sumndr(i) =  0
sumdr(i) =  0
sumdrab(i) =  0
}
doloop i from 1  to 8 step +1
{
sum(i) =  0
sumnodop(i) =  0
sumdop(i) =  0
eegdop(i) =  0
energyg1(i)=0
tg1(i) = 0
e11ca(i) =  0
e11cb(i) =  0
e11cc(i) =  0
e11cd(i) =  0
energyg2(i)=0
tg2(i) = 0
 x_1(i) =  0
 x_2(i) =  0
 x_3(i) =  0
 x_4(i) =  0
energyg3(i)=0
tg3(i) = 0
 y_1(i) =  0
```

```
 y_2(i) =  0
 y_3(i) =  0
 y_4(i) =  0
energyg4(i)=0
tg4(i) = 0
 z_1(i) =  0
 z_2(i) =  0
 z_3(i) =  0
 z_4(i) =  0
}
ns  =  0
nr  =  0
nga  =  0
ngb  =  0
ngc  =  0
ngd  =  0

createlist glist from clover
createlist slist from sect
createlist rlist from ring

gain glist.e1 segA factor 1.00
gain glist.e2 segB factor 1.00
gain glist.e3 segC factor 1.00
gain glist.e4 segD factor 1.00

loopif $g1=glist.e1 gt 0
{
  g = group($g1)
inc hitpatg(g)
energyg1(g)=$g1.e1
inc rclovera($g1.e1) indexed g
tg=timestampof($g1.e1)
tg1(g) = timestampof($g1.e1)
sum(g) = sum(g) + $g1.e1
}
loopif $g2=glist.e2 gt 0
{
  g = group($g2)
inc hitpatg(g)
energyg2(g)=$g2.e2
inc rcloverb($g2.e2) indexed g
tg=timestampof($g2.e2)
tg2(g) = timestampof($g2.e2)
sum(g) = sum(g) + $g2.e2
}
loopif $g3=glist.e3 gt 0
{
  g = group($g3)
inc hitpatg(g)
energyg3(g)=$g3.e3
inc rcloverc($g3.e3) indexed g
tg=timestampof($g3.e3)
tg3(g) = timestampof($g3.e3)
sum(g) = sum(g) + $g3.e3
}
loopif $g4=glist.e4 gt 0
{
  g = group($g4)
inc hitpatg(g)
energyg4(g)=$g4.e4
inc rcloverd($g4.e4) indexed g
tg=timestampof($g4.e4)
tg4(g) = timestampof($g4.e4)
sum(g) = sum(g) + $g4.e4
```

```
}

gain slist.e1 sect factor 1.00
gain rlist.e1 ring factor 1.00

!*****************************_BROAD_ENERGY_GATES_CONDITION_***************************

loopif $r=rlist.e1 passes (6500,16384)
{
  g = group($r) - 52
inc hitpatr(g)
energyr(g) = $r.e1
inc rings($r.e1) indexed g
tr = timestampof($r.e1)
tr1(g) = timestampof($r.e1)
  trr1 = tr1(g)
nr=nr + 1
}
loopif $s=slist.e1 passes (6500,16384)
{
  g = group($s) - 20
inc hitpats(g)
energys(g) = $s.e1
inc sectors($s.e1) indexed g
ts = timestampof($s.e1)
ts1(g) = timestampof($s.e1)
  tss1 = ts1(g)
ns=ns + 1
}
td=(ts-tr)+1024
inc timesi(td)
td=(tg-tr)+1024
inc timeg1(td)
td=(tg-ts)+1024
inc timeg2(td)
doloop iii from 1  to 32 step +1
{
es  =  energys(iii)
tss  =  ts
nsss  =  nss(iii)
if es gt 10
{
ss  =  iii
 es1  =  energys(ss)
}
}
if ns eq 1
 {
nsss  =  ns
 }
doloop ii from 1  to 24 step +1
{
er  =  energyr(ii)
trr  =  tr
nrrr  =  nrr(ii)
if er gt 10
{
rr  =  ii
imax  =  inelas_max(ii)
imin  =  inelas_min(ii)
er1  =  energyr(rr)
}
}
if nr eq 1
{
```

```
nrrr  =  nr
 }
c_si  =  nr + ns
td = (tss-trr) +1024
```

!***************************_PARTICLE_COINCIDENCE_CONDITION_***************************

```
if td passes (1015,1031)
{
if c_si eq 2
{
inc si_mat(es1/4,er1/4)
ee = ABS(es1-er1)
inc eeg(ee)
```

!********************************_ENERGY_SHARE_CONDITION_********************************

```
if ee lt  2500
{
inc si_matdc(es1/4,er1/4)
```

!********************************_INELASTIC_GATE_CONDITION_********************************

```
!if er1 lt  imax
! {
! if er1 gt  imin
!  {
```

!------------------------------------_DOPPLER_CORRECTION_------------------------------------

```
ee123  =  0
ecad  =  0
 ee312  =  0
ecbd  =  0
 ee321  =  0
eccd  =  0
ee213  =  0
ecdd  =  0
doloop i from 1 to 8 step +1
{
```

!--------------------_TRANSFORMATION_MATRIX_FOR_S3_DETECTOR_CRISTAL_A_------------

```
xb = d_target2s3*sin(sec_phi(ss))*sin(angdis(rr))
yb = d_target2s3*sin(angdis(rr))
zb = d_target2s3*cos(sec_phi(ss))*sin(angdis(rr))
ee123  =  energyg1(i)
if ee123 gt 0
{
```

!--------------------_TRANSFORMATION_MATRIX_FOR_GE_DETECTOR_CRISTAL_A_----------

```
x_1(i)=d_target2ge*sin(crys_a_phi(i))*sin(crys_a_theta(i))
xa  =  x_1(i)
y_1(i)=d_target2ge*cos(crys_a_theta(i))
ya  =  y_1(i)
z_1(i)=d_target2ge*cos(crys_a_phi(i))*sin(crys_a_theta(i))
za  =  z_1(i)
}
caa=(xa*xb+ya*yb+za*zb)/(sqrt(xa*xa+ya*ya+za*za)*sqrt(xb*xb+yb*yb+zb*zb))
```

!-------------------------------_ENERGY_DOPPLER_CORRECTED_CRYSTAL_A_----------------------

```
e11ca(i)=energyg1(i)*(1-beta(rr)*caa)/sqrt(1-beta(rr)*beta(rr))
ecad=e11ca(i)
```

69

```
tgg  =  tg1(i)
trr  =  tr1(rr)
tss  =  ts1(ss)
tdgs  =  (tgg - tss) +1024
tddd  =  (tgg - trr) +1024


!*****************_PARTICLE_GAMMA_COINCIDENCE_CONDITION_CRYSTAL_A_************

if tdgs passes (1035,1158)
 {
if tddd passes (1035,1158)
{
sumdr(rr)=sumdr(rr)+ecad
sumndr(rr)=sumndr(rr)+ee123
sumnodop(i)=sumnodop(i)+ee123
sumdop(i)=sumdop(i)+ecad
 }
}
ee312  =  energyg2(i)
if ee312 gt 0
{
x_2(i)=d_target2ge*sin(crys_b_phi(i))*sin(crys_b_theta(i))
xbb  =  x_2(i)
y_2(i)=d_target2ge*cos(crys_b_theta(i))
ybb  =  y_2(i)
z_2(i)=d_target2ge*cos(crys_b_phi(i))*sin(crys_b_theta(i))
zbb  =  z_2(i)
}
cab=(xbb*xb+ybb*yb+zbb*zb)/(sqrt(xbb*xbb+ybb*ybb+zbb*zbb)*sqrt(xb*xb+yb*yb+zb*zb))
e11cb(i)=energyg2(i)*(1-beta(rr)*cab)/sqrt(1-beta(rr)*beta(rr))
ecbd=e11cb(i)
tgg  =  tg2(i)
trr  =  tr1(rr)
tss  =  ts1(ss)
tdgs  =  (tgg - tss) +1024
tddd  =  (tgg - trr) +1024
if tdgs passes (1035,1158)
 {
if tddd passes (1035,1158)
 {
sumdr(rr)=sumdr(rr)+ecbd
sumndr(rr)=sumndr(rr)+ee312
sumnodop(i)=sumnodop(i)+ee312
sumdop(i)=sumdop(i)+ecbd
 }
}
ee321  =  energyg3(i)
if ee321 gt 0
{
x_3(i)=d_target2ge*sin(crys_c_phi(i))*sin(crys_c_theta(i))
xc  =  x_3(i)
y_3(i)=d_target2ge*cos(crys_c_theta(i))
yc  =  y_3(i)
z_3(i)=d_target2ge*cos(crys_c_phi(i))*sin(crys_c_theta(i))
zc  =  z_3(i)
}
cac=(xc*xb+yc*yb+zc*zb)/(sqrt(xc*xc+yc*yc+zc*zc)*sqrt(xb*xb+yb*yb+zb*zb))
e11cc(i)=energyg3(i)*(1-beta(rr)*cac)/sqrt(1-beta(rr)*beta(rr))
eccd=e11cc(i)
tgg  =  tg3(i)
trr  =  tr1(rr)
tss  =  ts1(ss)
tdgs  =  (tgg - tss) +1024
tddd  =  (tgg - trr) +1024
if tdgs passes (1035,1158)
```

70

```
 {
if tddd passes (1035,1158)
{
sumdr(rr)=sumdr(rr)+eccd
sumndr(rr)=sumndr(rr)+ee321
sumnodop(i)=sumnodop(i)+ee321
sumdop(i)=sumdop(i)+eccd
 }
}
ee213  =  energyg4(i)
if ee213 gt 0
{
x_4(i)=d_target2ge*sin(crys_d_phi(i))*sin(crys_d_theta(i))
xd  =  x_4(i)
y_4(i)=d_target2ge*cos(crys_d_theta(i))
yd  =  y_4(i)
z_4(i)=d_target2ge*cos(crys_d_phi(i))*sin(crys_d_theta(i))
zd  =  z_4(i)
}
cad=(xd*xb+yd*yb+zd*zb)/(sqrt(xd*xd+yd*yd+zd*zd)*sqrt(xb*xb+yb*yb+zb*zb))
e11cd(i)=energyg4(i)*(1-beta(rr)*cad)/sqrt(1-beta(rr)*beta(rr))
ecdd=e11cd(i)
tgg  =  tg4(i)
trr  =  tr1(rr)
tss  =  ts1(ss)
tdgs  =  (tgg - tss) +1024
tddd  =  (tgg - trr) +1024
if tdgs passes (1035,1158)
 {
if tddd passes (1035,1158)
 {
sumdr(rr)=sumdr(rr)+ecdd
sumndr(rr)=sumndr(rr)+ee213
sumnodop(i)=sumnodop(i)+ee213
sumdop(i)=sumdop(i)+ecdd
 }
}
sndop  =  sumnodop(i)
sndopr  =  sumndr(rr)
sdop  =  sumdop(i)
sdopr  =  sumdr(rr)
if sndop passes (1,16384)
 {
inc   ge_sum_no_dopplerr(sndop) indexed rr
inc   ge_sum_no_doppler(sndop)
 }
if sndopr passes (1,16384)
 {
inc   ge_sum_no_dopplerr2(sndopr) indexed rr
inc   ge_sum_no_doppler2(sndopr)
 }
if sdop passes (1,16384)
 {
inc   ge_sum_dopplerr(sdop) indexed rr
inc   ge_sum_doppler(sdop)
inc   eegdc(ee)
 }
if sdopr passes (1,16384)
 {
inc   ge_sum_dopplerr2(sdopr) indexed rr
inc   ge_sum_doppler2(sdopr)
 }
eegdop(i)=e11ca(i) + e11cb(i) + e11cc(i) + e11cd(i)
eegdop1  =  eegdop(i)
tddd  =  (tg - trr) +1024
```

71

```
tddd2  =  (tg - tss) +1024
sumdrab(rr)=sumdrab(rr)+eegdop1
sdopaddb  =  sumdrab(rr)
if sdopaddb passes (1,16364)
 {
inc   matdgr(tddd,sdopaddb)
inc   matdgs(tddd2,sdopaddb)
inc   ge_sum_doppleraddbb(sdopaddb)  indexed rr
inc   ge_sum_doppleraddb(sdopaddb)
 }
 }
 }
 }
}
!}
!}


*runfiles
!##########################_RUN_FILES_################################

DISC /home/elias/DATA/Good_data/PR256A/R6_0
DISC /home/elias/DATA/Good_data/PR256A/R7_0
DISC /home/elias/DATA/Good_data/PR256A/R8_0
DISC /home/elias/DATA/Good_data/PR256A/R9_0
DISC /home/elias/DATA/Good_data/PR256A/R10_0
DISC /home/elias/DATA/Good_data/PR256A/R11_0
DISC /home/elias/DATA/Good_data/PR256A/R12_0
DISC /home/elias/DATA/Good_data/PR256A/R13_0
DISC /home/elias/DATA/Good_data/PR256A/R14_0
DISC /home/elias/DATA/Good_data/PR256A/R15_0
DISC /home/elias/DATA/Good_data/PR256A/R16_0
DISC /home/elias/DATA/Good_data/PR256A/R17_0
DISC /home/elias/DATA/Good_data/PR256A/R18_0
DISC /home/elias/DATA/Good_data/PR256A/R19_0
DISC /home/elias/DATA/Good_data/PR256A/R20_0
DISC /home/elias/DATA/Good_data/PR256A/R21_0
DISC /home/elias/DATA/Good_data/PR256A/R22_0
DISC /home/elias/DATA/Good_data/PR256A/R23_0
DISC /home/elias/DATA/Good_data/PR256A/R24_0
DISC /home/elias/DATA/Good_data/PR256A/R25_0
DISC /home/elias/DATA/Good_data/PR256A/R26_0
DISC /home/elias/DATA/Good_data/PR256A/R27_0
DISC /home/elias/DATA/Good_data/PR256A/R28_0


*finish
```

Appendix B – Gosia Code.

Proj. integration .inp File: 194Pt(36Ar,36Ar*) @ 134.2 MeV:

```
OP,FILE
22,3,1
36Ar_excEEE.out
25,3,1
36Ar_excEEE.inp
9,3,1
det36Ar.gdt
0,0,0
OP,TITL
Proj. integration: 194Pt(36Ar,36Ar*) @ 134.2 MeV
OP,GOSI
LEVE
1,1,0,0.0
2,1,2,1.9704
3,1,4,4.414
0,0,0,0
ME
2,0,0,0,0
1,2,0.17352,1,1
2,2,0.2,1,1
2,3,0.2982,1,1
0,0,0,0,0
EXPT
24,18,36
-78,194,134.2,158.33,4,0,0,0,360,1,1       !1
.
.
.
-78,194,134.2,130.93,4,0,0,0,360,1,1       !24
CONT
SPL,1.
INT,24.
1,1000       ! 1
.
.
.
24,1000      ! 24
PRT,
1,0
2,0
4,0
5,1
11,0
12,0
14,0
16,0
18,1
0,0
END,

OP,YIEL
0
24,1
1.2, 1.3, 1.4, 1.5, 1.6, 1.7, 1.8, 1.9, 2.0, 2.1, 2.2, 2.3, 2.4, 2.5, 2.6, 2.7, 2.8, 2.9, 3.0, 3.1, 3.2, 3.3, 3.4, 3.5
2
5.33E-5, 6.59E-5, 8.62E-5, 0.0001155, 0.0001529, 0.000194, 0.000237, 0.000283, 0.000330, 0.000377,
0.000425, 0.000473, 0.000521, 0.000568, 0.000614, 0.000659, 0.000704, 0.000748, 0.000792, 0.000834,
0.000876, 0.000916, 0.000957, 0.000998
```

73

32,32,32,32,32,32,32,32,32,32,32,32,32,32,32,32,32,32,32,32,32,32,32,32 !24Exp and 32 G detectors per Experiment
1,1,1,1,1,1,1,1,1,1,1,1,1,1,1,1,1,1,1,1,1,1,1,1,1,1,1,1,1,1,1,1   ! 1
84.8,84.8,84.8,84.8,130.1,130.1,130.1,84.8,95.1,95.1,95.1,140.4,140.4,140.4,95.1,95.1,95.1,95.1,
140.4,140.4,140.4,95.1,84.8,84.8,84.8,84.8,130.1,130.1,130.1,84.8
95.1,49.8,230.3,320.3,5.2,275.0,49.8,275.0,95.1,49.8,230.3,320.3,5.2,275.0,49.8,275.0,84.8,39.5,220.0,310.0,
354.7,264.7,39.5,264.7,84.8,39.5,220.0,310.0,354.7,264.7,39.5,264.7
.
.
.
1,1,1,1,1,1,1,1,1,1,1,1,1,1,1,1,1,1,1,1,1,1,1,1,1,1,1,1,1,1,1,1   ! 32
84.8,84.8,84.8,84.8,130.1,130.1,130.1,84.8,95.1,95.1,95.1,95.1,140.4,140.4,140.4,95.1,95.1,95.1,95.1,95.1,
140.4,140.4,140.4,95.1,84.8,84.8,84.8,84.8,130.1,130.1,130.1,84.8
95.1,49.8,230.3,320.3,5.2,275.0,49.8,275.0,95.1,49.8,230.3,320.3,5.2,275.0,49.8,275.0,84.8,39.5,220.0,310.0,
354.7,264.7,39.5,264.7,84.8,39.5,220.0,310.0,354.7,264.7,39.5,264.7
2,1
32   !1
.1,.1,.1,.1,.1,.1,.1,.1,.1,.1,.1,.1,.1,.1,.1,.1,.1,.1,.1,.1,.1,.1,.1,.1,.1,.1,.1,.1,.1,.1,.1,.1
1.0000,1.0000,1.0000,1.0000,1.0000,1.0000,1.0000,1.0000,1.0000,1.0000,1.0000,1.0000,1.0000,1.0000,
1.0000,1.0000,1.0000,1.0000,1.0000,1.0000,1.0000,1.0000,1.0000,1.0000,1.0000,1.0000,1.0000,1.0000,
1.0000,1.0000,1.0000,1.0000
.
.
.
32   !24
.1,.1,.1,.1,.1,.1,.1,.1,.1,.1,.1,.1,.1,.1,.1,.1,.1,.1,.1,.1,.1,.1,.1,.1,.1,.1,.1,.1,.1,.1,.1,.1
1.0000,1.0000,1.0000,1.0000,1.0000,1.0000,1.0000,1.0000,1.0000,1.0000,1.0000,1.0000,1.0000,1.0000,
1.0000,1.0000,1.0000,1.0000,1.0000,1.0000,1.0000,1.0000,1.0000,1.0000,1.0000,1.0000,1.0000,1.0000,
1.0000,1.0000,1.0000,1.0000
0
0,0
2,1
2,0.473,0.029
3,0.110,0.014
0,0
0,0
OP,INTI
8, 6, 127.57, 134.21, 157.60, 159.06   !1
126.4, 127.7, 128.9, 130.2, 131.5, 132.8, 134.1, 135.3
.
.
.
8, 6, 127.57, 134.21, 130.57, 131.29   !24
126.4, 127.7, 128.9, 130.2, 131.5, 132.8, 134.1, 135.3
130.3, 130.5, 130.7, 130.9, 131.1, 131.4
14   !1
126.97,127.57,128.17,128.78,129.38,129.98,130.59,131.19,131.80,132.40,133.00,133.61,134.21,134.81
6.730,6.723,6.716,6.708,6.701,6.694,6.686,6.679,6.672,6.665,6.658,6.650,6.643,6.636
60,60
.
.
.
14   ! 24
126.97,127.57,128.17,128.78,129.38,129.98,130.59,131.19,131.80,132.40,133.00,133.61,134.21,134.81
6.730,6.723,6.716,6.708,6.701,6.694,6.686,6.679,6.672,6.665,6.658,6.650,6.643,6.636
60,60
OP,EXIT

Target excitation .inp File: 194Pt(36Ar,36Ar*) @ 134.2 MeV

```
OP,FILE
22,3,1
194pt_excEEE.out
25,3,1
194pt_excEEE.inp
9,3,1
det36Ar.gdt
0,0,0
OP,TITL
Target excitation: 194Pt(36Ar,36Ar*) @ 134.2 MeV
OP,GOSI
LEVE
1,1,0,0.0
2,1,2,0.3285
3,1,4,0.8114
4,1,6,1.4119
5,1,2,0.622
6,1,4,1.2295
0,0,0,0
ME
2,0,0,0,0
 1, 2,    1.208,1.0,1.4
 1, 5,    0.0888,0.08,0.1
 2, 5,    1.517,1.516,1.168
 2, 2,    0.54,0.4,0.8
 2, 3,    1.935,1.8,2.1
 2, 6,    0.13,0.1,0.2
 3, 3,    1.0,0.8,1.2
 3, 4,    2.90,2.8,3.1
 3, 5,    0.35,0.2,0.5
 3, 6,    1.35,1.2,1.5
 4, 4,    1.16,1.0,1.3
 4, 6,    0.40,0.3,0.5
 5, 5,    0.985,0.8,1.1
 5, 6,    1.637,1.5,1.8
 6, 6,    -0.83,-0.7,-1.0
7,0,0,0,0
 2, 5,    -0.093,-0.08,-0.12
 3, 6,    -0.245,-0.2,-0.3
0,0,0,0,0
EXPT
24,78,194
18,36,134.2,158.33,4,0,0,0,360,1,1        !1
.
.
.
18,36,134.2,130.93,4,0,0,0,360,1,1        !24
CONT
SPL,1.
INT,24.
1,1000!1
.
.
.
24,1000!24
PRT,
1,0
2,0
4,0
5,1
11,0
```

```
12,0
14,0
16,0
18,1
0,0
END,

OP,YIEL
1
6,2
0.2,0.3,0.4,0.5,0.6,0.7
2
0.359,0.0985,0.0438,0.0248,0.0161,0.01143
7
0.934,0.305,0.1407,0.0780,0.0484,0.0325
32,32,32,32,32,32,32,32,32,32,32,32,32,32,32,32,32,32,32,32,32,32,32,32        ! 24 Exp & 32 g detectors per experiment
1,1,1,1,1,1,1,1,1,1,1,1,1,1,1,1,1,1,1,1,1,1,1,1,1,1,1,1,1,1,1,1                      ! 1
84.8,84.8,84.8,84.8,130.1,130.1,130.1,84.8,95.1,95.1,95.1,95.1,140.4,140.4,140.4,95.1,95.1,95.1,95.1,95.1,
140.4,140.4,140.4,95.1,84.8,84.8,84.8,84.8,130.1,130.1,130.1,84.8
95.1,49.8,230.3,320.3,5.2,275.0,49.8,275.0,95.1,49.8,230.3,320.3,5.2,275.0,49.8,275.0,84.8,39.5,220.0,310.0,
354.7,264.7,39.5,264.7,84.8,39.5,220.0,310.0,354.7,264.7,39.5,264.7
.
.
.
1,1,1,1,1,1,1,1,1,1,1,1,1,1,1,1,1,1,1,1,1,1,1,1,1,1,1,1,1,1,1,1                      ! 32
84.8,84.8,84.8,84.8,130.1,130.1,130.1,84.8,95.1,95.1,95.1,95.1,140.4,140.4,140.4,95.1,95.1,95.1,95.1,95.1,
140.4,140.4,140.4,95.1,84.8,84.8,84.8,84.8,130.1,130.1,130.1,84.8
95.1,49.8,230.3,320.3,5.2,275.0,49.8,275.0,95.1,49.8,230.3,320.3,5.2,275.0,49.8,275.0,84.8,39.5,220.0,310.0,
354.7,264.7,39.5,264.7,84.8,39.5,220.0,310.0,354.7,264.7,39.5,264.7
2,1
32         !1
.1,.1,.1,.1,.1,.1,.1,.1,.1,.1,.1,.1,.1,.1,.1,.1,.1,.1,.1,.1,.1,.1,.1,.1,.1,.1,.1,.1,.1,.1,.1,.1
1.0000,1.0000,1.0000,1.0000,1.0000,1.0000,1.0000,1.0000,1.0000,1.0000,1.0000,1.0000,1.0000,1.0000,1.0000,
1.0000,1.0000,1.0000,1.0000,1.0000,1.0000,1.0000,1.0000,1.0000,1.0000,1.0000,1.0000,1.0000,1.0000,1.0000,
1.0000,1.0000
.
.
.
32         !24
.1,.1,.1,.1,.1,.1,.1,.1,.1,.1,.1,.1,.1,.1,.1,.1,.1,.1,.1,.1,.1,.1,.1,.1,.1,.1,.1,.1,.1,.1,.1,.1
1.0000,1.0000,1.0000,1.0000,1.0000,1.0000,1.0000,1.0000,1.0000,1.0000,1.0000,1.0000,1.0000,1.0000,1.0000,
1.0000,1.0000,1.0000,1.0000,1.0000,1.0000,1.0000,1.0000,1.0000,1.0000,1.0000,1.0000,1.0000,1.0000,1.0000,
1.0000,1.0000
0
0,0
2,1
2,60.9,2.7
3,50.5,5.8
0,0
0,0
OP,INTI
8, 6, 127.57, 134.21, 157.60, 159.06         !1
126.4, 127.7, 128.9, 130.2, 131.5, 132.8, 134.1, 135.3
157.3, 157.7, 158.1, 158.5, 158.9, 159.3
.
.
.
8, 6, 127.57, 134.21, 130.57, 131.29         !24
126.4, 127.7, 128.9, 130.2, 131.5, 132.8, 134.1, 135.3
130.3, 130.5, 130.7, 130.9, 131.1, 131.4
14         !1
126.97,127.57,128.17,128.78,129.38,129.98,130.59,131.19,131.80,132.40,133.00,133.61,134.21,134.81
6.730,6.723,6.716,6.708,6.701,6.694,6.686,6.679,6.672,6.665,6.658,6.650,6.643,6.636
60,60
```

.
.
.
14   ! 24
126.97,127.57,128.17,128.78,129.38,129.98,130.59,131.19,131.80,132.40,133.00,133.61,134.21,134.81
6.730,6.723,6.716,6.708,6.701,6.694,6.686,6.679,6.672,6.665,6.658,6.650,6.643,6.636
60,60
OP,EXIT

Appendix C

Research proposal presented to the PAC at iThemba LABS

1. A RESEARCH PROPOSAL TO THE iThemba LABS:
   PHYSICAL SCIENCES RESEARCH PROGRAM ON SSC FACILITY

2. ZIG ZAG OF NUCLEAR SHAPES AT THE END OF THE SD SHELL

3. 17 SEPTEMBER 2015

4. MEMBERS OF GROUP

- Makabata Mokgolobotho, Craig Mehl, M. Kumar Raju, Nicholas Erasmus, Smarajit Triambak, Bhivek Singh, Luthendo Phuthu, Vicente Pesudo, Daniel Lambarri, Bernadette Rebeiro, Werner Richter and Nico Orce (coulex@gmail.com), University of the Western Cape.

- Mathis Wiedeking, Vincent Kheswa, Peter Jones, Tshepo Dinoko, Elena Lawrie, Ntombi Kheswa, Jacobus Lawrie, Rudolph Nchodu, Rainer Thomae and the iThemba LABS Nuclear Physics Group.

- Paul Papka, Preston Vymers, J.J. van Zyl and Phil Adsley, Stellenbosch University.

- Sifiso Ntshangase, University of Zululand.

- John L. Wood, Georgia Institute of Technology, USA.

- Gordon Ball, TRIUMF, Canada.

- P. -H. Heenen, Université Libre de Bruxelles, Belgium.

5. ABSTRACT

We propose the determination of the spectroscopic quadrupole moments, Q_s, for the 2_1^+ and (at least the sign of) higher-lying 2^+ states in ^{32}S and ^{36}Ar using Coulomb-excitation reorientation-effect (RE) measurements. The accepted $Q_s(2_1^+)_{RE}$ values for these nuclides in the NNDC are poorly (^{36}Ar) and ambiguously (^{32}S) determined and comparison with state-of-the-art mean-field models is fruitless. Our measurements will utilise ^{32}S and ^{36}Ar beams at safe energies, with a minimum distance between nuclear surfaces of $S(\theta_{c.m.})_{min}$ = 6.6 fm, impinging onto a 0.5 mg/cm^2 ^{208}Pb target. The accurate determination of $Q_s(2^+)_{RE}$ values in these nuclei will shed light onto the presumed vibrational pattern observed in ^{32}S, shape evolution and shape coexistence in the region, and the breaking of the $N = Z = 20$ shell closures.

6. EMPHASIS

(a) Pure basic research	90 %
(b) Directed basic research	0%
(c) Applied research	0%
(d) Experimental development, services	10 %

7. SCIENTIFIC MOTIVATION

A remarkable feature of atomic nuclei is their ability to adopt different mean field shapes for a small cost in energy compared to their total binding energy. The nucleus ^{40}Ca is spherical in its ground state and doubly magic with the $N = Z = 20$ gap energy being about 7 MeV. Positive parity states are expected at least twice that energy. The finding of its first excitation (0_2^+ state) being as low as 3.35 MeV [1] originated, together with similar deformed bands in ^{16}O [2, 3], the phenomenon of shape coexistence [4]. The deformed bands in ^{16}O were explained by the promotion of pairs of protons and neutrons across the $N = Z = 8$ closed shells [4, 5, 6, 7]. The structure of the deformed bands in ^{40}Ca corresponds to the promotion of 4 particles-4 holes ($4p - 4h$) and 8 particles-8 holes ($8p - 8h$) from the sd to the pf shell, across the Fermi level. Large-scale shell-model [8] and beyond mean-field [9, 10] calculations explain the ex-

Figure 1: Overall comparison of experiment and theory for $Q_s(2_1^+)$ values in the sd shell [11].

treme lowering in energy of these excited 0^+ states through the mixing of different 0^+ configurations. In a cluster picture, these $4p - 4h$ and $8p - 8h$ excitations are associated with the ^{36}Ar $+ \alpha$ and ^{32}S $+ 2\alpha$ cluster configurations, respectively.

A Zig-Zag of Confusion

A rapidly shape changing scenario as a function of proton and/or neutron number is found in sd-shell nuclei [11]. Figure 1 shows the variation of $Q_s(2_1^+)$ values in the sd shell as a function of mass number. The experimentally determined $Q_s(2_1^+)$ values in ^{20}Ne, ^{24}Mg and ^{32}S [$Q_s(2_1^+) < 0$] indicate prolate shapes, whereas $Q_s(2_1^+)$ values in ^{28}Si and ^{36}Ar [$Q_s(2_1^+) > 0$] represent oblate shapes. An intriguing zig-zag pattern is observed at the end of the sd shell starting from a prolate shape in ^{26}Mg. A self-consistent HFBCS Nilsson diagram for neutrons (similar for protons) is shown in Fig. 2 for the region of interest, and illustrates the richness of shell gaps as a function of quadrupole deformation [9]. The first goal of this proposal is to *unambiguously characterise the pattern of alternate shapes* by determining the $Q_s(2_1^+)$ values in ^{32}S and ^{36}Ar.
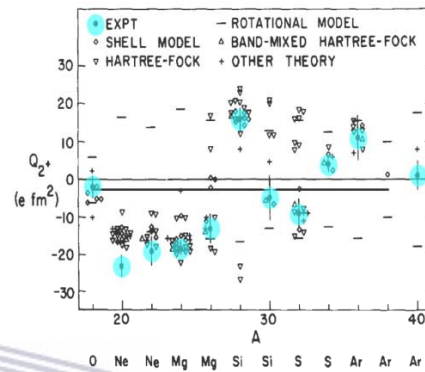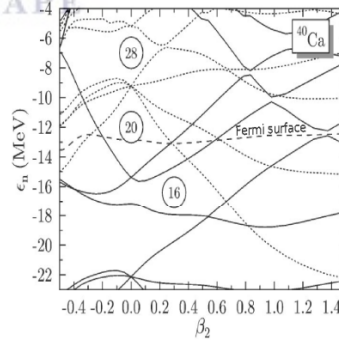

Figure 2: Self-consistent HFBCS Nilsson diagram for neutrons. Figure taken from [9].
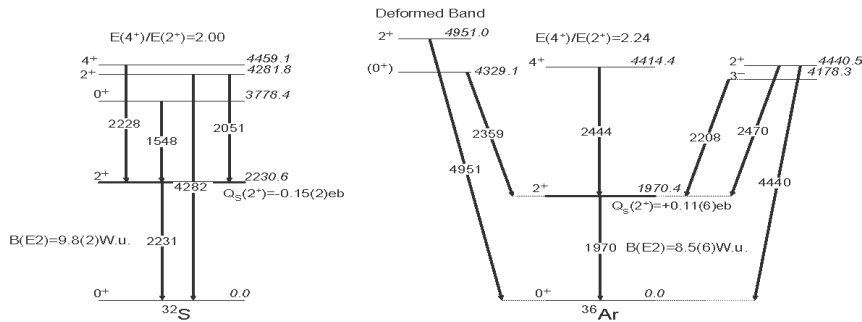
Figure 3: Low-lying level schemes of ^{32}S and ^{36}Ar. The 0^+_2 excitation in ^{36}Ar [15] is the band head of a deformed band; whereas the excitation energies of the 0^+_2, 2^+_2 and 4^+_1 states in ^{32}S correspond to a spherical vibrator. $B(E2)$ and $Q_s(2^+_1)_{RE}$ values are taken from [12] and [13], respectively.

Deformed Bands and Shape Coexistence

Figure 3 shows the low-lying level schemes of ^{32}S and ^{36}Ar. By looking at the rapidly changing shell structure in Fig. 2, it is not surprising that shape coexistence [14] has recently been identified in ^{36}Ar [15] and ^{40}Ar [16] with deformed bands built on the 0^+_2 excitations. The level scheme of ^{32}S corresponds, however, to that of a quadrupole vibrator [17]; with a suspiciously large $Q_s(2^+_1)_{RE} = -15(2)$ efm^2. Shape coexistence has not been identified in ^{32}S.

Previous studies led to an indirect inference of nuclear shapes based on energy ratios, changes in the moment of inertia and the comparison of measured $B(E2)$ values with calculations. Regarding shape coexistence, it is relevant to determine precisely the nuclear shapes and answer the following questions: 1) *Is there shape mixing between the 0^+ excitations?*, or similarly, *how does the nuclear shape evolve with excitation energy and gives rise to deformed bands and shape coexistence?* and 2) *Are the added clusters to the ^{32}S and ^{36}Ar cores and/or large ground-state oblate or prolate shapes responsible for breaking the $N = Z = 20$ shell closure?* Surprisingly, even nowadays, the $Q_S(2^+_1)_{RE}$ values in these nuclei remain poorly (^{36}Ar) and ambiguously (^{32}S) determined.

Poor Measurements of $Q_s(2^+_1)_{RE}$ Values

Strikingly, there is only one *RE* measurement of $Q_S(2^+_1)_{RE}$ for ^{36}Ar [18], with $Q_S(2^+_1)_{RE} = +11(6)$ efm^2 (oblate with 55% uncertainty). This value is most likely perturbed by effects of nuclear interference. In their measurements, Nakai and collaborators used a suspiciously small minimum separation between nuclear surfaces, $S(\theta_{c.m.})_{min} = 4.3$ fm for ^{36}Ar. The importance of using larger $S(\theta_{c.m.})_{min}$ values was established afterwards as a measure to avoid nuclear interference [11, 19, 20]. For light nuclei, an acceptable compromise for the minimum distance of closest approach d_{min} between projectile and target nuclei is,

$$d_{min} \gtrsim 1.25(A_p^{1/3} + A_T^{1/3}) + 6.4 \text{ fm}, \tag{1}$$

where 6.4 fm is the minimum separation between nuclear surfaces, $S(\theta_{c.m.})_{min}$.

80

Moreover, the analyses of Nakai *et al.* for ^{36}Ar involved assumptions about the $E2$ matrix elements of the target nuclei. In particular, it was assumed that $Q_s(2^+_1)_{RE} = 0.0 \pm 0.5 \mid Q_s(2^+_1)_{B(E2)} \mid$. Nevertheless, a later RE measurement in ^{206}Pb determined $Q_s(2^+_1)_{RE} = 0.17 \pm 0.31 \mid Q_s(2^+_1)_{B(E2)} \mid$ [21, 22]. As outlined by Spear in his 1981 review article: *"Further experimental work is clearly desirable for each of these nuclei (^{36}Ar and ^{40}Ar), particularly with experimental techniques different from those already used."* This single measurement of $Q_s(2^+_1)_{RE} = +11(6)$ efm^2 for ^{36}Ar still stands as the accepted value in the $NNDC$ nuclear database [22].

For ^{32}S, the accepted $Q_s(2^+_1)_{RE}$ value in the $NNDC$ nuclear database indicates a prolate shape and is accepted as $Q_s(2^+_1)_{RE} = -0.154(20)$ [22]. Nevertheless, this value arise from the weighted average of four RE measurements already discussed in Spear's review article. There, Spear concluded that *"The values of $S(\theta_{c.m.})_{min}$ for the early experiments of Nakai et al. [23] and Häusser et al. [24] are so small that their results are almost certainly perturbed by effects of nuclear interference. It seems best simply to adopt the unweighted mean of the results of Olin et al. [25] and Ball et al. [26], and to assign an error which takes account of the spread of the results. A further measurement of $Q_s(2^+_1)_{RE}$ for ^{32}S is highly desirable."* Such a measurement was never performed and Spear's adopted value of $Q_s(2^+_1)_{RE} = -9(4)$ efm^2 ignored.
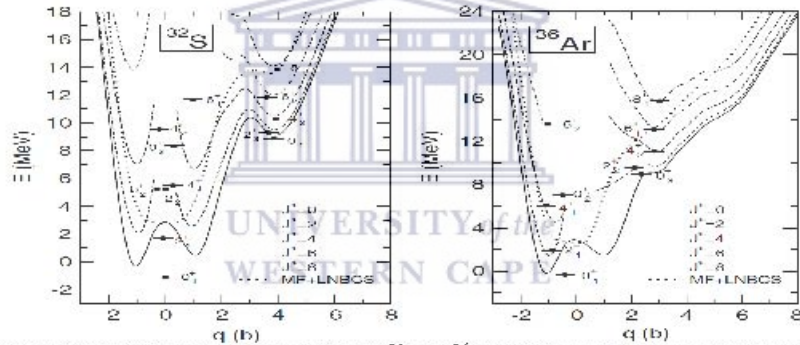

Figure 4: Beyond RPA mean-field calculations for ^{32}S and ^{36}Ar [10]. The mean-field energy curves display an spherical and a rather flat oblate minimum, respectively.

Theoretically, it is difficult to adopt or improve a particular model or interaction because of the poorly determined $Q_s(2^+_1)_{RE}$ values. With a potentially large prolate shape ($Q_s(2^+_1)_{RE} = +11(6)$ efm^2), the 2^+_1 state in ^{36}Ar lies quite high at 1.970 MeV, as shown in the level schemes of Fig. 3. An additional confusing scenario arises when comparing $Q_s(2^+_1)_{RE}$ values with theory. State-of-the-art beyond RPA mean-field calculations using the relativistic point-coupling interaction PC-F1 are presented in Fig. 4 for ^{32}S (left) and ^{36}Ar (right) [10]. Similar results are obtained by Bender and co-workers using the non-relativistic beyond mean-field model and the Skyrme interaction [9]. For ^{32}S, a slightly oblate and an almost spherical shape for $Q_s(2^+_1)$ are calculated, respectively, by the beyond the relativistic mean-field ($Q_s(2^+_1)_{theory} = +5.8$ efm^2) and beyond mean-field ($Q_s(2^+_1)_{theory} = +2.3$ efm^2) models. A closer result to the accepted value ($Q_s(2^+_1)_{RE} = -15(2)$ efm^2) is obtained by Rodríguez-Guzmán and collaborators ($Q_s(2^+_1)_{theory} = -13.29$ efm^2) using the Gogny D1S effective interation [27]. The ambiguity of the experimental value prevents further conclusions.

The theoretical comparison of the $Q_s(2_1^+)_{RE}$ value in ^{36}Ar seems more agreeable with data. Although the calculated 2_1^+ energy is almost 1 MeV higher with the beyond mean-field model, both mean-field approaches yield the same oblate shape with $Q_s(2_1^+)_{theory} = +13$ efm^2. Again, the uncertainty of the experimental value prevents further conclusions. Caurier and co-workers, using large-scale shell-model calculations for ^{36}Ar, agree with the experimental excitation energies but discrepancies arise for the calculated $B(E2)$ values [28]. No calculations of $Q_s(2_1^+)$ were carried out by Caurier and co-workers. Accurate determinations of $Q_s(2_1^+)_{RE}$ for ^{32}S and ^{36}Ar will provide a deep insight into the development of deformation in this region of the nuclear chart and serve as a stringent test for timely state-of-the-art mean-field calculations.

8. EXPERIMENTAL TECHNIQUES AND EQUIPMENT

We aim at determining the $Q_s(2_1^+)_{RE}$ values for the 2_1^+ states in ^{32}S and ^{36}Ar using Coulomb-excitation reorientation effect measurements. Beams of ^{32}S and ^{36}Ar are currently available at iThemba LABS, where SF$_6$ and enriched ^{36}Ar gas bottles can be injected in the HMI ion source. Maximum safe energies of 121.5 MeV for ^{32}S beams and 138 MeV for ^{36}Ar beams will be utilised, respectively. These beams will be bombarding a 0.5-1 mg/cm^2 thick ^{208}Pb target. The de-excited γ-rays will be detected using the AFRODITE clover detector array [29], which comprises nine HPGe clover detectors; with five clovers at 90° and four clovers at 135° in the standard configuration. The scattered particles will be detected in coincidence with γ-rays using a double-sided silicon CD-type S3 detector at backward angles (shown in Fig. 5) and a W2 double-sided silicon detector at forward angles. The S3 detector contains 24 rings (for angular distributions) and 16 sectors (for Doppler correction) and the target to detector distance will be 40 mm, which will cover an angular range w.r.t to the beam axis of [138.8° − 164.0°]. The W2 double-sided silicon detector has 16x16 elements but no axial symmetry and will

Figure 5: A double-sided (CD-type) S3 silicon detector placed upstream in the AFRODITE chamber during the RE measurements with ^{40}Ar beams last April 2015.

be placed at forward angles with an angular range w.r.t to the beam axis of [45° − 75°]. Such measurements will run at a maximum current of ≈ 0.5 pnA to avoid detector damage at forward angles. A thin 0.5-1 mg/cm^2 ^{208}Pb target will minimize Doppler broadening. The γ-ray energies will be Doppler corrected based on the coincidences with the particle detectors. In this way, relatively good energy resolution can be maintained. The feasibility of these kind of experiments has been confirmed by recent measurements with ^{40}Ar beams carried out last April 2015 (see PR181 and PR247 reports attached) at iThemba LABS. A report on the status of the PR247 experiment will be presented during the next PAC meeting at the end of October 2015. Caution with the particle-γ coincidence timing in the digital electronics system is crucial as this is the main source of experimental failure in most facilities.

The safe energies are calculated for the chosen projectile and target combination system using Eq. 2, which satisfies the condition of minimum distance between nuclear surfaces $S(\theta_{c.m.})_{min} \approx 6.5$ fm suggested by Kean [19] and Spear [11].

$$S(\theta_{c.m.}) = \frac{0.72 Z_1 Z_2}{E}(1 + \frac{A_1}{A_2})[1 + cosec(\frac{1}{2}\theta_{C.M})] - 1.25(A_1^{1/3} + A_2^{1/3}) \text{ fm}. \tag{2}$$

Figure 6 shows the variation of safe distances between nuclear surfaces as a function of the scattering forward angles in the laboratory frame for the ^{208}Pb(^{36}Ar,^{36}Ar*)^{208}Pb* reaction. The beam energy of E_{lab}=138 MeV corresponds to the safe energy for $S(\theta_{c.m.})_{min}$= 6.6 fm. The requested beam energies given above are calculated similarly.

The $Q_S(2_1^+)$ value in ^{32}S and ^{36}Ar will be determined from γ-ray data and by comparing with the semiclassical coupled-channel Coulomb-excitation code GOSIA [30]. The Sommerfeld parameter is $\eta = \frac{a}{\lambda} > 100$ for the Coulomb-excitation reactions considered in this proposal; where a is the half-distance of closest approach, $\lambda = \frac{\hbar}{p}$ the de Broglie wavelength. A Sommerfeld parameter of $\eta \gg 1$ validates the semiclassical approximation and nuclear interference can be considered negligible.
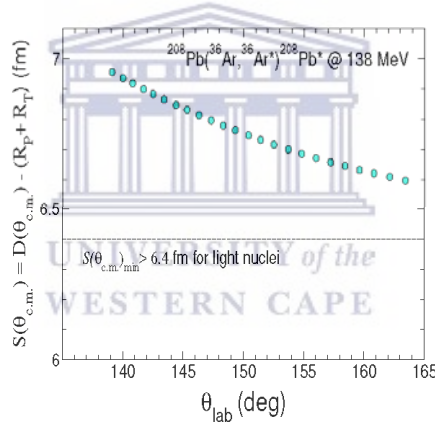

Figure 6: Distance between nuclear surfaces, $S(\theta_{c.m.})$ as a function projectile scattering angle in the laboratory frame for the ^{208}Pb(^{36}Ar,^{36}Ar*)^{208}Pb* reaction at 138 MeV. The data points correspond to the average angles for the 24 rings that compose the S3 double-sided silicon detector placed upstream 40 mm from the target position.

GOSIA determines γ-ray yields for given matrix elements. For a $J^\pi = 2^+$ state, the spectroscopic quadrupole moment is related to the diagonal matrix element, $\langle 2_1^+ \parallel E2 \parallel 2_1^+ \rangle$ by,

$$\begin{aligned} Q_S(2_1^+) &= \sqrt{\frac{16\pi}{5}} \frac{1}{\sqrt{2J+1}} \langle JJ20 \mid JJ \rangle \langle 2_1^+ \parallel E2 \parallel 2_1^+ \rangle \\ &= 0.75793 \langle 2_1^+ \parallel E2 \parallel 2_1^+ \rangle. \end{aligned} \tag{3}$$

The population of different magnetic substates changes with Q_s and may enhance ($Q_s(2_1^+) > 0$) or inhibit ($Q_s(2_1^+) < 0$) the asymmetry of the angular distribution of the de-excitation γ-rays. With sufficient statistics, this change in the angular distribution provides an accurate spectroscopic probe for a measurement of Q_s. The magnitude of the *RE* is given by the product of the transitional and diagonal matrix elements in Eq. 4. For accelerated ions, the use of high-Z targets enhances the *RE* because of the stronger time-dependent field gradient [20].

$$
\begin{aligned}
\sigma_{E2} = \quad & \sigma_R \quad \kappa_1(\theta_{CM}, \xi) \, |\langle 2_1^+ \, \| \, E2 \, \| \, 0_1^+ \rangle|^2 \\
\times \quad & (\, 1 + \kappa_2(\theta_{CM}, \xi) \, \langle 2_1^+ \, \| \, E2 \, \| \, 2_1^+ \rangle \,),
\end{aligned}
\tag{4}
$$

where σ_R is the Rutherford scattering cross section and $\kappa_1(\theta_{CM}, \xi)$, $\kappa_2(\theta_{CM}, \xi)$ are the Coulomb-excitation coefficients known from perturbation theory [31]; the latter depend on the scattering angle, θ_{CM}, in the center-of-mass frame and the adiabaticity parameter, $\xi = \frac{\tau_{collision}}{\tau_{nuclear}}$, i.e., the ratio between the collision time and the lifetime of the nuclear level.

The determination of $\langle 2_i^+ \, \| \, E2 \, \| \, 2_i^+ \rangle$ matrix elements in ^{32}S and ^{36}Ar can be achieved by normalizing the γ-ray yields to their well-known $B(E2; 2_1^+ \rightarrow 0_1^+)$ values to account for experimental unknowns in the setup, such as the systematic uncertainties in the absolute beam energy, target thickness, particle detection efficiency and dead time of the data acquisition.

In addition, the total Coulomb-excitation cross sections for projectile (P) and target (T) can be related by,

$$
\frac{\sigma_{E2}^T}{\sigma_{E2}^P} \frac{W(\theta)^T}{W(\theta)^P} = \frac{N_\gamma^T}{N_\gamma^P} \frac{\varepsilon_\gamma^P}{\varepsilon_\gamma^T} = \frac{I_\gamma^T}{I_\gamma^P},
\tag{5}
$$

where, ε_γ^T and ε_γ^P are the relative γ-ray efficiencies and $W(\theta)$ represents the integrated angular distribution of the de-excited γ-rays. This method has been used by Orce and collaborators for a pure ^{10}Be beam [32] and it is useful fo the low statistics typically found with radioactive ion beams or populating higher-lying states.

Count rate estimates

A GOSIA simulation of the ^{208}Pb(^{36}Ar,^{36}Ar*)^{208}Pb* reaction at 138 MeV, using two double-sided $S3$ detectors at forward and backward angles, an $\approx$1% efficiency for a 2 MeV γ-ray with the AFRODITE array, estimates a cross section of $\approx$2 mb for the population of the 2_1^+ state in ^{36}Ar. With a 0.2 pnA intensity, and a target thickness of 1 mg/cm^2, two weekends of beam time will give of the order of 40,000 counts for the 2_1^+ peak in ^{36}Ar. Similar yields are obtained for the population of the 2_1^+ state in ^{32}S. Therefore, two weekends of beam time for each nucleus would be sufficient to carry out these measurements. More detailed calculations, including γ-ray yield angular distributions, will be presented during the PAC meeting at the end of October 2015. The data analysis will be done by students from the MaNus Honours/MSc programme at UWC.

References

[1] A. M. Nathan and J. J. Kolata, Phys. Rev. C **14**, 171 (1976).

[2] E. B. Carter, G. E. Mitchell, and R. H. Davis, Phys. Rev. **133**, B1421 (1964).

[3] P. Chevallier, F. Scheibling, G. Goldring, I. Plesser, and M.W. Sachs, Phys. Rev. **160**, 827 (1967).

[4] H. Morinaga, Phys. Rev. **101**, 254 (1956).

[5] G. E. Brown, in Comptes Rendus du Congres International de Physique Nucleaire de Paris (Editions du Centre National de la Recherche Scientifique, Paris), Vol. 1, 129 (1964).

[6] G. E. Brown and A. M. Green, Nucl. Phys. **75**, 401 (1966).

[7] G. E. Brown and A. M. Green, Nucl. Phys. **85**, 87 (1966).

[8] E. Caurier, J. Menéndez, F. Nowacki and A. Poves, Phys. Rev. C **75**, 054317 (2007).

[9] M. Bender, H. Flocard, and P. -H. Heenen, Phys. Rev. C **68**, 044321 (2003).

[10] T. Nikšić, D. Vretenar and P. Ring, Phys. Rev. C **74**, 064309 (2006).

[11] R. H. Spear, Phys. Rep. **73**, 369 (1981).

[12] B.Pritychenko, M.Birch, M.Horoi, B.Singh, Nucl. Data Sheets **120,** 112 (2014).

[13] N. J. Stone, At. Data Nucl. Data Tables **90**, 75 (2005).

[14] K. Heyde and J. L. Wood, Rev. Mod. Phys. **83**, 1467 (2011).

[15] C. E. Svensson *et al.*, Phys. Rev. Lett. **85**, 13 (2000).

[16] E. Ideguchi *et al.*, Phys. Lett. **B686** 18 (2010).

[17] A. Bohr and B.R. Mottelson, *Nuclear Structure V.II*, World Scientific Publishing Company (1998).

[18] K. Nakai, F. S. Stephens and R.M. Diamond, Phys. Lett. **34B**, 389 (1971).

[19] D. C. Kean, Lecture Notes in Physics (Springer), Volume **92**, 80 (1976).

[20] O. Häusser, in Nuclear Spectroscopy and Reactions, edited by J. Cerny (1974), Part C, p. 55.

[21] A.M.R. bye, A. M. Baxter, S. Hinds, D. C. Keats and R. H. Spear, Phys. Lett. **72B**, 307 (1978).

[22] D. R. Tilley, H. R. Weller and G. M. Hale, Nucl. Phys. A **541**, 1 (1992); http://www.nndc.bnl.gov/

[23] K. Nakai, IL. Québert, F. S. Stephens and R. M. Diamond, Phys. Rev. Lett. **24**, 903 (1970).

[24] 0. Häusser, T.K. Alexander, A.B. McDonald and W.T. Diamond, Nucl. Phys. A**175**, 593 (1971).

[25] A. Olin, 0. Häusser, T.K. Alexander, A.J. Ferguson and W. Witthuhn, Nucl. Phys. A**221**, 555 (1974).

[26] G.C. Ball *et al.*, Nucl. Phys. A**349**, 271 (1980).

[27] R. R. Rodriguéz-Guzmán, J. L. Egido and L. M. Robledo, Phys. Lett. B**474**, 15 (2000).

[28] E. Caurier, F. Nowacki and A. Poves, Phys. Rev. Lett. **95**, 042502 (2005).

[29] M. Lipoglavsek *et al.*, Nucl. Instr. Meth. Phys. Res., **A557**, 523 (2006).

[30] T. Czosnyka, D. Cline, and C.Y. Wu, Bull. Am. Phys. Soc. **28**, 745 (1983); (see also 2011 GOSIA manual).

[31] K. Alder and A. Winther, *Electromagnetic Excitation* (North-Holland, Amsterdam, 1975).

[32] J.N. Orce *et al.* Phys. Rev. C **86**, 041303(R) (2012).

9. COST ESTIMATE

The double-sided S3 and W2 detectors, the enriched ^{208}Pb material and ^{36}Ar bottle have already been purchased and are readily available.

10. BEAM REQUIREMENTS

^{32}S beams at a maximum energy of 121.5 MeV and ≈ 0.5 pnA intensity. ^{36}Ar beams at a maximum energy of 138 MeV and ≈ 0.5 pnA intensity.

11. ESTIMATE OF RUNNING TIME

From GOSIA simulations given above, two weekends per nucleus are requested to determine the $\langle 2_1^+ \parallel E2 \parallel 2_1^+ \rangle$ matrix elements in ^{32}S and ^{36}Ar. A total of four weekends.

12. SCHEDULING INFORMATION

We would like to request the beam time at the beginning of 2016 to allow our MSc students to finish their degrees on time.

13. SAFETY

No peculiar safety requirements.

14. SIGNATURES OF PRINCIPAL RESEARCHERS

Nico Orce

Bibliography

[1] K. Nakai, F.S. Stephens, and R.M. Diamond, Phys. Lett. B 34, issue 5, 389 (1971).

[2] National Nuclear DataCenter http://www.nndc.bnl.gov/

[3] R. H. Spear, Phys. Rep. 73, 369 (1981).

[4] K. Heyde and J. L. Wood, Rev. Mod. Phys. 83, 1467 (2011).

[5] K. Alder, F. Roesel and R. Morf, Second-order quantum-Mechanical Theory of Coulomb Excitation (1972).

[6] K. Alder, A. Bohr Study of Nuclear Structure by Electromagnetic Excitation with accelerated Ions, Rev. Mod. Phys. 28, 433 (1967).

[7] D. C. Kean, Lecture Notes in Physics (Springer) 92, 80 (1976).

[8] Krishna Kumar, Phys. Rev. Lett. 28, 249 (1972).

[9] Douglas Cline, Ann. Rev. Nucl. Part. Sci. 36, 683(1986).

[10] O. Hausser, in Nuclear Spectroscopy and Reactions, edited by J. Cerny (Academic, New York, 1974), Part C, p.55.

[11] E. Rutherford. The scattering of α and β Particles by Matter and the Structure of the Atom. Philos. Mag. 21, 669 (1911).

[12] J. de Boer, J. Eichler, Adv. Nucl. Phys. (Springer) 1, 1 (1968).

[13] D. Schwalm et al, Nul. Phys. A 192, 449 (1972).

[14] K. Alder and A. Winther, Coulomb Excitation, Academic Press, New York (1966).

[15] T. Czosnyka, D.Cline and C. Y. Wu, GOSIA manual (2012); www.pas. rochester.edu/~cline/Gosia/Gosia_Manual_20120510.pdf

[16] A. Lell, Diplomarbeit, Sektion Physik, Universität Müchen and J. de Boer, Treatise on Heavy-ion Science, Vol. 1, Plenum Press, 293 (1984).

[17] A. Bohr and B. R. Mottelson, Nuclear Structure Vol. II: Nuclear Deformations, World Scientific Publishing Co. Pte. Ltd. (1998).

[18] A. Bohr and B. R. Mottelson, Kgl. Danske Videnskab. Selskab, Mat.-FyS. Medd. 27, 16 (1953).

[19] National Research Foundation, http://www.nrf.ac.za/

[20] A. Ostrowski, S. Cherubini et al., CD: A double sided silicon strip detectorfor radioactive nuclear beam experiments, Nucl. Instr. Meth. A480, 448 (2002).

[21] MIDAS Website: http://npsg.dl.ac.uk/MIDAS/

[22] Radware Website: https://radware.phy.ornl.gov/.

[23] Qian Yue and Zeng Zhi from Tsinghua University. The characteristics of a low background germanium gamma ray spectrometer at China JinPing underground Laboratory (2014).

[24] J.N. Orce et al., Phys. Rev. C 86, 041303(R) (2012).

[25] K. Adler, A. Bohr, T. Huus, B. Mottelson, A. Winther, Rev. Mod. Phys. 28, 432 (1956).

[26] B. Pritychenko, M. Birch, B. Singh, M. Horoi, At. Data Nucl. Data Tables 107, 1 (2016).

[27] D. J. Rowe, Nuclear Collective Motion (1970).

[28] R. R. Rodriguez-Guzman, J. L. Egido and L. M. Robledo, Phys. Lett. B 474, 15 (2000).

[29] E. Caurier, F. Nowacki and A. Poves, Phys. Rev. Lett. 95, 042502 (2005).